Spectral Method Applied to Turbulent Reentry Flows Submitted to Magnetic Field in 2D: Seven Species

Edisson Sávio de Góes Maciel

Rua Santa Clara, 245 – Cx. Postal: 2029 – 12.243-970 – São José dos Campos – SP – Brazil

Abstract In the present work, a study involving a spectral method to solve the reactive Favre averaged Navier-Stokes equations, coupled with a turbulence model and the Maxwell equations, is performed. The Favre averaged Navier-Stokes equations coupled with the Maxwell equations, in conservative and finite volume contexts, employing structured spatial discretization, are studied. Turbulence is taken into account considering the implementation of five k-ω two-equation turbulence models, based on the works of Coakley 1983; Wilcox; Yoder, Georgiadids and Orkwis; Coakley 1997; and Rumsey, Gatski, Ying, and Bertelrud. For the magnetic formulation, the Gaitonde model is implemented. The Euler backward integration method is studied to march the scheme in time. The spectral method presented in this work employs collocation points and variants of Chebyshev and Legendre interpolation functions are studied. The "hot gas" hypersonic flow around a blunt body in two-dimensions is simulated. The convergence process is accelerated to steady state condition through a spatially variable time step procedure, which has proved effective gains in terms of computational acceleration (see Maciel). The reactive simulations involve Earth atmosphere chemical model of seven species and eighteen reactions, based on the Blottner model. N, O, N_2, O_2, NO, NO^+ and e^- species are used to perform the numerical comparisons. The results have indicated that the Chebyshev collocation point variants are more accurate in terms of stagnation pressure estimations. For the studied problem such errors are inferior to 3.68%, being 1.93% the best result. The Legendre collocation point variants are more accurate in terms of the lift coefficient estimations. Moreover, the Legendre collocation point variants are more computationally efficient and cheaper.

Keywords Spectral method; Hypersonic flow; Thermochemical non-equilibrium reentry flows; Euler and Navier-Stokes equations; Maxwell equations; High order accuracy; Maciel scheme.

1. Introduction

There are several approaches for computationally modeling fluid dynamics. These include finite difference, finite element, and spectral methods to name a few. Finite element and finite difference methods are frequently used and offer a wide range of well-known numerical schemes. These schemes can vary in terms of computational accuracy but are typically of lower order of accuracy. If a more accurate solution is desired, it is common practice to refine the mesh either globally or in a region of interest. This can often be a complicated or time consuming process as global mesh refinement will greatly increase the computation time while local refinement requires an elaborated refinement operation [1].

Alternatively, polynomial refinement has been used to improve the solution accuracy and has been shown to converge more quickly than mesh refinement in some cases [2-3]. For finite difference methods, polynomial refinement is performed by including neighboring node values in a higher order polynomial [4]. This can increase the complexity of the scheme especially near the boundaries where nodes do not exist to construct the higher order polynomials. Finite element methods instead increase the number of unknown values within the cell itself to construct a higher order solution [5].

A scheme with a very high formal order of accuracy will not necessarily always produce the highest resolution. [6] demonstrated that a spectral-like scheme with a formal fourth-order accuracy produced a much more highly resolved solution than schemes with higher formal orders of accuracy when comparing modified wave numbers. Therefore, formal order of accuracy does not provide a comprehensive basis for selecting the best solution procedure. State-of-art methods such as spectral methods fall into this category.

Spectral methods are considered a class of solution techniques using sets of known functions to solve differential equations [7]. Such methods are generally considered high order and capable of obtaining solutions with a high resolution. Unlike finite-difference and finite-element methods, spectral methods utilize an expansion in terms of global, rather than local, basis functions to represent the solution of a differential equation. When properly applied, these techniques accurately resolve phenomena on the scale of the mesh spacing. The order of truncation error decay with mesh refinement is also higher than which can be achieved with finite-difference and finite-element methods. For problems with smooth solutions, it is possible to produce spectral method whose truncation error goes to zero as faster than any finite power of the mesh spacing (exponential convergence).

Spectral methods may be viewed as an extreme development of the class of discretization schemes known by the generic name of method of weighted residuals (MWR) [8]. The key elements of the MWR are the trial functions (also called the expansion or approximating functions) and the test functions (also known as weighted functions). The trial functions are used as the basis functions for a truncated series expansion of the solution that, when substituted into the differential equation, produces the residual. The test functions are used to enforce the minimization of the residual.

The choice of the trial functions is what distinguishes the spectral methods from the element and finite difference methods. The trial functions for spectral methods are infinitely differentiable global functions (Typically, they are tensor products of the eigenfunctions of singular Sturm-Liouville problems). In the case of finite element methods, the domain is divided into small elements and a trial function is specified in each element. The trial functions are thus local in character and well suited for handling complex geometries. The finite difference trial functions are likewise local.

The choice of test function distinguishes between Galerkin and collocation approaches. In the Galerkin approach, the test functions are the same as the trial functions, whereas in the collocation approach the test functions are translated Dirac delta functions. In other words, the Galerkin approach is equivalent to a least-square approximation, whereas the collocation approach requires the differential equations to be solved exactly at the collocation points.

The collocation approach is the simplest of the MWR and appears to have been first used by [9] in his study of electronic energy bands in metals. A few years later, [10] applied this method to the problem of torsion in square prism. [11] developed it as a general method for solving ordinary differential equations. They used a variety of trials functions and an arbitrary distribution of collocation points. The work of [12] established for the first time that a proper choice of the trial functions and the distribution of collocation points is crucial to the accuracy of the solution. Perhaps he should be credited with laying down the foundation of the orthogonal collocation method.

Spectral methods have been used on one-dimensional, compressible flow problems with piecewise linear solutions by [13-14]. These reports demonstrated that spectral methods, when combined with appropriate filtering techniques, can capture one-dimensional shock waves in otherwise featureless flows. A different sort of demonstration was provided by [15]. They exhibited spectral solutions of compressible flows with nontrivial structures in the smooth regions.

Renewed interest in the area of hypersonic flight has brought Computational Fluid Dynamics (CFD) to the forefront of fluid flow research [16]. Many years have seen a quantum leap in advancements made in the areas of computer systems and software which utilize them for problem solving. Sophisticated and accurate numerical algorithms are devised routinely that are capable of handling complex computational problems. Experimental test facilities capable of addressing complicated high-speed flow problems are still scarce because they are too expensive to build and sophisticated measurements techniques appropriate for such problems, such as the non-

intrusive laser, are still in the development stage. As a result, CFD has become a vital tool in the flow problem solution.

In high speed flows, any adjustment of chemical composition or thermodynamic equilibrium to a change in local environment requires certain time. This is because the redistribution of chemical species and internal energies require certain number of molecular collisions, and hence a certain characteristic time. Chemical non-equilibrium occurs when the characteristic time for the chemical reactions to reach local equilibrium is of the same order as the characteristic time of the fluid flow. Similarly, thermal non-equilibrium occurs when the characteristic time for translation and various internal energy modes to reach local equilibrium is of the same order as the characteristic time of the fluid flow. Since chemical and thermal changes are the results of collisions between the constituent particles, non-equilibrium effects prevail in high-speed flows in low-density air.

In chemical non-equilibrium flows the mass conservation equation is applied to each of the constituent species in the gas mixture. Therefore, the overall mass conservation equation is replaced by as many species conservation equations as the number of chemical species considered. The assumption of thermal non-equilibrium introduces additional energy conservation equations – one for every additional energy mode. Thus, the number of governing equations for non-equilibrium flow is much bigger compared to those for perfect gas flow. A complete set of governing equations for non-equilibrium flow may be found in [17-18].

The problems of chemical non-equilibrium in the shock layers over vehicles flying at high speeds and high altitudes in the Earth's atmosphere have been discussed by several investigators [19-22]. Most of the existing computer codes for calculating the non-equilibrium reacting flow use the one-temperature model, which assumes that all of the internal energy modes of the gaseous species are in equilibrium with the translational mode [21-22]. It has been pointed out that such a one-temperature description of the flow leads to a substantial overestimation of the rate of equilibrium because of the elevated vibrational temperature [20]. A three-temperature chemical-kinetic model has been proposed by [23] to describe the relaxation phenomena correctly in such a flight regime. However, the model is quite complex and requires many chemical rate parameters which are not yet known. As a compromise between the three-temperature and the conventional one-temperature model, a two-temperature chemical-kinetic model has been developed [24-25], which is designated herein as the TTv model. The TTv model uses one temperature T to characterize both the translational energy of the atoms and molecules and the rotational energy of the molecules, and another temperature Tv to characterize the vibrational energy of the molecules, translational energy of the electrons, and electronic excitation energy of atoms and molecules. The model has been applied to compute the thermodynamic properties behind a normal shock wave in a flow through a constant-area duct [24-25]. Radiation emission from the non-equilibrium flow has been calculated using the Non-equilibrium Air Radiation (NEQAIR) program [26-27]. The flow and the radiation computations have been packaged into a single computer program, the Shock-Tube Radiation Program (STRAP) [25].

In spite of the advances made in the area of compressible turbulence modeling in recent years, no universal turbulence model, applicable to such complex flow problems has emerged so far. While the model should be accurate it should also be economical to use in conjunction with the governing equations of the fluid flow. Taking these issues into consideration, k-ω two-equation models have been chosen in the present work [28-32]. These models solve differential equations for the turbulent kinetic energy and the vorticity. Additional differential equations for the variances of temperature and species mass fractions have also been included. These variances have been used to model the turbulence-chemistry interactions in the reacting flows studied here.

The effects associated with the interaction of magnetic forces with conducting fluid flows have been profitably employed in several applications related to nuclear and other [33] technologies and are known to be essential in the explanation of astrophysical phenomena. In recent years, however, the study of these interactions has received fresh impetus in the effort to solve the problems of high drag and thermal loads encountered in hypersonic flight. The knowledge that electrical and magnetic forces can have profound influence on hypersonic flow fields is not new [34-35]– note increased shock-standoff and reduced heat transfer rates in hypersonic flows past blunt bodies under the application of appropriate magnetic fields. The recent interest stems, however, from new revelations of a Russian concept vehicle, known as AJAX [36], which made extensive reference to technologies requiring tight coupling between electromagnetic and fluid dynamic phenomena. A

magnetogasdynamics (MGD) generator was proposed [37] to extract energy from the incoming air while simultaneously providing more benign flow to combustion components downstream. The extracted energy could then be employed to increase thrust by MGD pumping of the flow exiting the nozzle or to assist in the generation of plasma for injection of the body. This latter technique is known to not only reduce drag on the body but also to provide thermal protection [38].

In addition to daunting engineering challenges, some of the phenomena supporting the feasibility of an AJAX type vehicle are fraught with controversy (see, for example, [39]). Resolution of these issues will require extensive experimentation as well as simulation. The latter approach requires integration of several disciplines, including fluid dynamics, electromagnetics, chemical kinetics, and molecular physics amongst others. This paper describes a recent effort to integrate the first three of these, within the assumptions that characterize ideal and non-ideal magnetogasdynamics.

In the present work, a study involving a spectral method to solve the reactive Favre averaged Navier-Stokes equations, coupled with a turbulence model and the Maxwell equations, is performed. The Favre averaged Navier-Stokes equations coupled with the Maxwell equations, in conservative and finite volume contexts, employing structured spatial discretization, are studied. Turbulence is taken into account considering the implementation of five k-ω two-equation turbulence models, based on the works of [28-32]. For the magnetic formulation, the [40-41] model is implemented. The Euler backward integration method is studied to march the scheme in time. The spectral method presented in this work employs collocation points and variants of Chebyshev and Legendre interpolation functions are studied. The "hot gas" hypersonic flow around a blunt bodyin two-dimensions is simulated. The convergence process is accelerated to steady state condition through a spatially variable time step procedure, which has proved effective gains in terms of computational acceleration [42-43]. The reactive simulations involve Earth atmosphere chemical model of seven species and eighteen reactions, based on the [44] model. N, O, N_2, O_2, NO, NO^+ and e^- species are used to perform the numerical comparisons. The Maciel scheme is used to perform the numerical experiments. The results have indicated that the Chebyshev collocation point variants are more accurate in terms of stagnation pressure estimations. For the studied problem such errors are inferior to 3.68%, being 1.93% the best result. The Legendre collocation point variants are more accurate in terms of the lift coefficient estimations. Moreover, the Legendre collocation point variants are more computationally efficient and cheaper.

2. Spectral Method

Two classes of techniques for spectral discretization are referred to as tau and collocation methods [45]. The latter technique is used here. In this scheme, the approximation series is determined by satisfying the differential equation exactly at a set of distinct collocation points. The locations of these points in the domain are linked to the choice of basis function. In this study, arbitrary collocation points are implemented. The collocation method is used here since enforcement of boundary conditions and evaluations of nonlinear terms are straightforward. Additionally, some accuracy advantage is seen in the collocation method over the tau method for a number of problems [45]. The series expansion for a function $Q(x)$ may be represented as

$$Q_N(x) = \sum_{n=0}^{N} \hat{Q}_n B_n(x),$$
(1)

Where $B_n(x)$ are the basis functions and N is the total number of nodes employed in the interpolation process (it is also the order of accuracy of the spectral method). The coefficients $\hat{Q}_n$ are often termed the spectrum of $Q_N(x)$. One common technique used to evaluate the spectrum is to consider Eq. (1) as an interpolation series representing $Q(x)$. The interpolation "nodes" of such series are the collocation points of the method. For a scheme based on Chebyshev collocation, the basis functions are:

$$B_n(x) = T_n(x) = 2xP_{n-1}(x) - P_{n-2}(x), \qquad n \geq 2,$$
(2)

with: $P_0(x) = 1$ and $P_1(x) = x$. The Chebyshev-Gauss-Lobatto standard collocation points are

$$x_1 = \cos\left(\frac{\pi l}{N}\right), \qquad l = 0, 1, \ldots, N.$$
(3)

The Chebyshev collocation points result from a simple change of variables, which relates the Chebyshev interpolation series to a Fourier cosine series [45]. To evaluate the $\hat{Q}_n$, the inverse relation is required. This is

$$\hat{Q}_n = \hat{c}_n \sum_{l=0}^{N} w_l B_n(x_l) Q_{i,j}, \qquad n = 0, 1, \ldots, N, \tag{4}$$

With w_l being a normalized weighting function and $\hat{c}_n$ a constant. These variables assume the following expressions to a Chebyshev-Gauss-Lobatto interpolation:

$$\hat{c}_n = \frac{2}{N\overline{c}_n}, \text{ where: } \overline{c}_n = \begin{cases} 2, & n = 0 \text{ or } N \\ 1, & 1 < n < N-1 \end{cases}; \text{ and } w_l = \frac{1}{\overline{c}_l}. \tag{5}$$

Legendre collocation is based on using Legendre polynomials as the basis function in Eq. (1), e.g.,

$$B_n(x) = \left[(2n-1)xP_{n-1}(x) - (n-1)P_{n-2}(x)\right]/n, \qquad n \geq 2, \tag{6}$$

where: $P_0(x) = 1$ and $P_1(x) = x$. Interpolation via Legendre series cannot easily be related to trigonometric interpolation, so there is no simple expression to evaluate the $\hat{Q}_n$ coefficients. Appeal must be made to the theory of numerical quadrature to form an approximation to the integrals which result from analytic Legendre interpolation [46]. Considering Eq. (4), the normalized weights and constant of the Legendre-Gauss-Lobatto collocation points are

$$w_l = \frac{1}{N(N+1)B_N^2(x_l)} \text{ and } \hat{c}_n = \begin{cases} 2n+1, & n = 0,1,\ldots,N-1 \\ N, & n = N \end{cases}. \tag{7}$$

In this work, it was assumed that the Legendre-Gauss-Lobatto collocation points are the same as the Chebyshev-Gauss-Lobatto ones. It was also adopted the following collocation points and normalized weight for the Chebyshev-Gauss-Radau interpolation, based on the work of [47]:

$$x_l = \cos\left(\frac{2\pi l}{2N+1}\right), \tag{8}$$

$$w_l = \begin{cases} \dfrac{N}{2N+1}, & l = 0 \\ \dfrac{N}{N+1}, & \text{elsewhere} \end{cases}. \tag{9}$$

For the Legendre-Gauss-Radau interpolation, also based in [47], the collocation points are defined by Eq. (8) and the normalized weights are described by:

$$w_l = \begin{cases} \dfrac{1}{(N+1)^2}, & l = 0 \\ \dfrac{1}{2(N+1)^2} \times \dfrac{1-x_l}{B_N(x_l)}, & \text{elsewhere} \end{cases}. \tag{10}$$

The same calculation to the vector of conserved variables Q is applied to the vector of flux C, to be defined in section 6.

Hence, we have two collocation point options and two normalized weight functions to be considered by the Chebyshev and the Legendre methods, namely: Chebyshev-Gauss-Radau, Chebyshev-Gauss-Lobatto, Legendre-Gauss-Radau and Legendre-Gauss-Lobatto.

3. Favre Average

The Navier-Stokes equations and the equations for energy and species continuity which governs the flows with multiple species undergoing chemical reactions have been used [48-50] for the analysis. Details of the present implementation for the seven species chemical model, and the specification of the thermodynamic and transport properties are described in [51-52]. Density-weighted averaging [53] is used to derive the turbulent flow

equations from the above relations. For a detailed description of the Favre equations, the g's equations and the modeling are presented in [54]. The interested reader is encouraged to read this paper.

4. Favre-averaged Navier-Stokes Equations Coupled with Maxwell Equations

The flow is modeled by the Favre-averaged Navier-Stokes equations coupled with the Maxwell equations and the condition of thermochemical non-equilibrium, where the rotational and vibrational contributions are considered, is taken into account. The reactive Navier-Stokes equations in thermal and chemical non-equilibrium were implemented on conservative and finite volume contexts, in the two-dimensional space. In this case, these equations in integral and conservative forms can be expressed by:

$$\frac{\partial}{\partial t}\int_V Q dV + \int_S \vec{F} \bullet \vec{n} dS = \int_V S_{CV} dV + \int_V G dV, \text{ with: } \vec{F} = \left(E_e - E_v\right)\vec{i} + \left(F_e - F_v\right)\vec{j}, \tag{11}$$

where: Q is the vector of conserved variables, V is the volume of a computational cell, $\vec{F}$ is the complete flux vector, $\vec{n}$ is the unity vector normal to the flux face, S is the flux area, G is the k-ω two-equation model source term, S_{CV} is the chemical and vibrational source term, E_e and F_e are the convective flux vectors or the Euler flux vectors in the x and y directions, respectively, and E_v and F_v are the viscous flux vectors in the x and y directions, respectively. The $\vec{i}$ and $\vec{j}$ unity vectors define the Cartesian coordinate system. Seventeen (17) conservation equations are solved: one of general mass conservation, two of linear momentum conservation, one of total energy, six of species mass conservation, one of the vibrational internal energy of the molecules, two of the k-ω turbulence model, two of the g-equations, and two of the Maxwell equations. Therefore, one of the species is absent of the iterative process. The CFD literature recommends that the species of biggest mass fraction of the gaseous mixture should be omitted, aiming to result in a minor numerical accumulation error. To the present study, in which is chosen a chemical model to the air composed of seven (7) chemical species (N, O, N_2, O_2, NO, NO^+ and e^-) and eighteen chemical reactions to the [44] model, this species can be the N_2 or the O_2. To this work, the N_2 was chosen. The vectors Q, E_e, F_e, E_v, F_v, G and S_{CV} can, hence, be defined as follows:

$$Q = \begin{Bmatrix} \rho \\ \rho u \\ \rho v \\ \rho Z \\ \rho_1 \\ \rho_2 \\ \rho_4 \\ \rho_5 \\ \rho_6 \\ \rho_7 \\ \rho e_V \\ \rho k \\ \rho \omega \\ \rho Q_h \\ \rho Q_s \\ B_x \\ B_y \end{Bmatrix}, E_e = \begin{Bmatrix} \rho u \\ \rho u^2 + P - R_b\,B_x^2/\mu_M \\ \rho uv - R_b\,B_x B_y/\mu_M \\ \left(\rho Z + P\right)u - R_b\left(\vec{V} \bullet \vec{B}/\mu_M\right)B_x \\ \rho_1 u \\ \rho_2 u \\ \rho_4 u \\ \rho_5 u \\ \rho_6 u \\ \rho_7 u \\ \rho e_V u \\ \rho k u \\ \rho \omega u \\ \rho Q_h u \\ \rho Q_s u \\ 0 \\ uB_y - vB_x \end{Bmatrix}, F_e = \begin{Bmatrix} \rho v \\ \rho uv - R_b\,B_x B_y/\mu_M \\ \rho v^2 + P - R_b\,B_y^2/\mu_M \\ \left(\rho Z + P\right)v - R_b\left(\vec{V} \bullet \vec{B}/\mu_M\right)B_y \\ \rho_1 v \\ \rho_2 v \\ \rho_4 v \\ \rho_5 v \\ \rho_6 v \\ \rho_7 v \\ \rho e_V v \\ \rho k v \\ \rho \omega v \\ \rho Q_h v \\ \rho Q_s v \\ vB_x - uB_y \\ 0 \end{Bmatrix}, \tag{12}$$

in which: ρ is the mixture density; u and v are Cartesian components of the velocity vector in the x and y directions, respectively; $\vec{V}$ is the complete flow velocity vector; P is the pressure term considering the magnetic effect; Z is the fluid total energy considering the contribution of the magnetic field; $\vec{B}$ is the complete magnetic field vector; R_b is the magnetic force number or the pressure number; ρ_1, ρ_2, ρ_4, ρ_5, ρ_6 andρ_7 are densities of the N, O, O_2, NO, NO^+, and e^-, respectively; k is the turbulent kinetic energy; ω is the turbulent vorticity; Q_h is the product of fluctuating enthalpy, $\overline{h^{''}h^{''}}$; Q_s is the sum of the product of fluctuating mass fraction, $\sum_{i=1}^{ns}\overline{c_i^{''}c_i^{''}}$;B_x and

B_y are Cartesian components of the magnetic field vector in the x and y directions, respectively; μ_M is the mean magnetic permeability, with the value of $4\pi\text{x}10^{-7}$T·m/A; e_V is the sum of the vibrational energy of the molecules; the τ's are the components of the Reynolds stress tensor; the t's are the components of the viscous stress tensor; f_x and f_y are viscous work and Fourier heat flux functions; $\rho_s v_{sx}$ and $\rho_s v_{sy}$ represent the species diffusion flux, defined by the Fick law; ϕ_x and ϕ_y are the terms of mixture diffusion; $\phi_{v,x}$ and $\phi_{v,y}$ are the terms of molecular diffusion calculated at the vibrational temperature; α_x, α_y, β_x, β_y, γ_x, γ_y, δ_x and δ_y are two-equation turbulence model parameters; θ_{sx} and θ_{sy} are diffusion terms function of the mass fraction gradients; $\dot{\omega}_s$ is the chemical source term of each species equation, defined by the law of mass action; e_v^* is the molecular-vibrational-internal energy calculated with the translational/rotational temperature;

$$
E_v = \left\{ \begin{array}{c}
0 \\
(t_{xx}+\tau_{xx})/\text{Re} \\
(t_{xy}+\tau_{xy})/\text{Re} \\
(f_x-\phi_x)/\text{Re}-q_{J,x}/\text{Re}_\sigma \\
(-\rho_1 v_{1x}-\theta_{1x})/\text{Re} \\
(-\rho_2 v_{2x}-\theta_{2x})/\text{Re} \\
(-\rho_4 v_{4x}-\theta_{4x})/\text{Re} \\
(-\rho_5 v_{5x}-\theta_{5x})/\text{Re} \\
(-\rho_6 v_{6x}-\theta_{6x})/\text{Re} \\
(-\rho_7 v_{7x}-\theta_{7x})/\text{Re} \\
(q_{v,x}-\phi_{v,x})/\text{Re} \\
\alpha_x/\text{Re} \\
\beta_x/\text{Re} \\
\gamma_x/\text{Re} \\
\delta_x/\text{Re} \\
0 \\
\frac{1}{\text{Re}_\sigma}\frac{1}{\sigma}\left[\frac{\partial}{\partial x}\left(\frac{B_y}{\mu_M}\right)-\frac{\partial}{\partial y}\left(\frac{B_x}{\mu_M}\right)\right]
\end{array} \right\},\quad
F_v = \left\{ \begin{array}{c}
0 \\
(t_{xy}+\tau_{xy})/\text{Re} \\
(t_{yy}+\tau_{yy})/\text{Re} \\
(f_y-\phi_y)/\text{Re}-q_{J,y}/\text{Re}_\sigma \\
(-\rho_1 v_{1y}-\theta_{1y})/\text{Re} \\
(-\rho_2 v_{2y}-\theta_{2y})/\text{Re} \\
(-\rho_4 v_{4y}-\theta_{4y})/\text{Re} \\
(-\rho_5 v_{5y}-\theta_{5y})/\text{Re} \\
(-\rho_6 v_{6y}-\theta_{6y})/\text{Re} \\
(-\rho_7 v_{7y}-\theta_{7y})/\text{Re} \\
(q_{v,y}-\phi_{v,y})/\text{Re} \\
\alpha_y/\text{Re} \\
\beta_y/\text{Re} \\
\gamma_y/\text{Re} \\
\delta_y/\text{Re} \\
\frac{1}{\text{Re}_\sigma}\frac{1}{\sigma}\left[\frac{\partial}{\partial y}\left(\frac{B_x}{\mu_M}\right)-\frac{\partial}{\partial x}\left(\frac{B_y}{\mu_M}\right)\right] \\
0
\end{array} \right\};
\tag{13}
$$

$$
S_{CV} = \left\{\begin{array}{c} 0 \\ 0 \\ 0 \\ 0 \\ \dot{\omega}_1 \\ \dot{\omega}_2 \\ \dot{\omega}_4 \\ \dot{\omega}_5 \\ \dot{\omega}_6 \\ \dot{\omega}_7 \\ \sum_{s=mol}\rho_s\left(e^{*}_{v,s}-e_{v,s}\right)/\tau_s + \sum_{s=\omega}\dot{\omega}_s e_{v,s} \\ 0 \\ 0 \\ 0 \\ 0 \\ 0 \\ 0 \end{array}\right\} ;\quad
G = \left\{\begin{array}{c} 0 \\ 0 \\ 0 \\ 0 \\ 0 \\ 0 \\ 0 \\ 0 \\ 0 \\ 0 \\ 0 \\ G_k \\ G_\omega \\ \left(\dfrac{2\mu_T}{Re\,Pr\,d_T}\right)\left[\left(\dfrac{\partial h}{\partial x}\right)^2 + \left(\dfrac{\partial h}{\partial y}\right)^2\right] \\ \left(\dfrac{2\mu_T}{Re\,Sc_T}\right)\left[\left(\dfrac{\partial c_T}{\partial x}\right)^2 + \left(\dfrac{\partial c_T}{\partial y}\right)^2\right] + \dfrac{\Psi}{Re} \\ 0 \\ 0 \end{array}\right\} ;\qquad (14)
$$

τ_s is the translational-vibrational characteristic relaxation time of each molecule; $q_{v,x}$ and $q_{v,y}$ are the vibrational Fourier heat flux components in the x and y directions, respectively; Re is the laminar Reynolds number; $q_{J,x}$ and $q_{J,y}$ are the components of the Joule heat flux vector in the x and y directions, respectively; Re_σ is the magnetic Reynolds number; σ is the electrical conductivity; G_k and G_ω are k-ω source terms; μ_T is the turbulent viscosity or vorticity viscosity; h is the static enthalpy; and c_T is the total mass fraction sum.

The viscous stresses, in N/m^2, are determined, according to a Newtonian fluid model, by:

$$
t_{xx} = \left[2\mu_m\,\partial u/\partial x - 2/3\mu_m\left(\partial u/\partial x + \partial v/\partial y\right)\right] ;
$$
$$
t_{xy} = \mu_m\left(\partial u/\partial y + \partial v/\partial x\right); \qquad (15)
$$
$$
t_{yy} = \left[2\mu_m\left(\partial v/\partial y\right) - 2/3\mu_m\left(\partial u/\partial x + \partial v/\partial y\right)\right],
$$

where μ_m is the molecular viscosity. The components of the turbulent stress tensor (Reynolds stress tensor) are described by the following expressions:

$$
\tau_{xx} = \left[2\mu_T\,\partial u/\partial x - 2/3\mu_T\left(\partial u/\partial x + \partial v/\partial y\right)\right] - 2/3 Re\rho k ;
$$
$$
\tau_{xy} = \mu_T\left(\partial u/\partial y + \partial v/\partial x\right); \qquad (16)
$$
$$
\tau_{yy} = \left[2\mu_T\,\partial v/\partial y - 2/3\mu_T\left(\partial u/\partial x + \partial v/\partial y\right)\right] - 2/3 Re\rho k .
$$

Expressions to f_x and f_y are given below:

$$
f_x = \left(t_{xx} + \tau_{xx}\right)u + \left(t_{xy} + \tau_{xy}\right)v + q_x + q_{v,x} + k_x ; \qquad (17)
$$
$$
f_y = \left(t_{xy} + \tau_{xy}\right)u + \left(t_{yy} + \tau_{yy}\right)v + q_y + q_{v,y} + k_y , \qquad (18)
$$

where q_x and q_y are the Fourier heat flux components and are given by:

$$q_x = \left(\mu_m/Prd_L + \mu_T/Prd_T\right)\partial h/\partial x;$$ (19)

$$q_y = \left(\mu_m/Prd_L + \mu_T/Prd_T\right)\partial h/\partial y,$$ (20)

where: Prd_L and Prd_T are the laminar and turbulent Prandtl numbers. The $q_{v,x}$ and $q_{v,y}$ are the vibrational heat flux components and are given by:

$$q_{v,x} = k_V\,\partial T_V/\partial x;$$ (21)

$$q_{v,y} = k_V\,\partial T_V/\partial y,$$ (22)

with k_V being the vibrational thermal conductivity and T_V is the vibrational temperature, what characterizes this model as of two temperatures: translational/rotational and vibrational. The last terms in Eqs. (17)-(18) are k_x and k_y and are defined as follows:

$$k_x = \left(\mu_m + \frac{\mu_T}{\sigma_k}\right)\partial k/\partial x\,;\text{ and } k_y = \left(\mu_m + \frac{\mu_T}{\sigma_k}\right)\partial k/\partial y.$$ (23)

The diffusion terms related to the k-ω equations are defined as:

$$\alpha_x = \left(\mu_m + \mu_T/\sigma_k\right)\partial k/\partial x,\ \alpha_y = \left(\mu_m + \mu_T/\sigma_k\right)\partial k/\partial y\,;$$ (24)

$$\beta_x = \left(\mu_m + \mu_T/\sigma_\omega\right)\partial\omega/\partial x,\ \beta_y = \left(\mu_m + \mu_T/\sigma_\omega\right)\partial\omega/\partial y\,;$$ (25)

$$\gamma_x = \left(\mu_m/Prd_L + \mu_T/Prd_T\right)\partial Q_h/\partial x,\ \gamma_y = \left(\mu_m/Prd_L + \mu_T/Prd_T\right)\partial Q_h/\partial y\,;$$ (26)

$$\delta_x = \left(\mu_m/Sc + \mu_T/Sc_T\right)\partial Q_S/\partial x,\ \delta_y = \left(\mu_m/Sc + \mu_T/Sc_T\right)\partial Q_S/\partial y,$$ (27)

with: Sc and Sc_T are the laminar and turbulent Schmidt numbers, with values 0.22 and 1.00, respectively. The terms of species diffusion, defined by the Fick law, to a condition of thermal non-equilibrium, are determined by [55]:

$$\rho_s v_{sx} = -\rho D_s\frac{\partial Y_{MF,s}}{\partial x}\text{ and }\rho_s v_{sy} = -\rho D_s\frac{\partial Y_{MF,s}}{\partial y}\,,$$ (28)

with "s" referent to a given species, $Y_{MF,s}$ being the molar fraction of the species, defined as:

$$Y_{MF,s} = \frac{\rho_s/M_s}{\displaystyle\sum_{k=1}^{ns}\rho_k/M_k}$$ (29)

and D_s is the species-effective-diffusion coefficient and "ns" the total number of species.

The diffusion terms ϕ_x and ϕ_y which appear in the energy equation are defined by [56]:

$$\phi_x = \sum_{s=1}^{ns}\rho_s v_{sx}h_s\text{ and }\ \phi_y = \sum_{s=1}^{ns}\rho_s v_{sy}h_s\,,$$ (30)

being h_s the specific enthalpy (sensible) of the chemical species "s". The molecular diffusion terms calculated at the vibrational temperature, $\phi_{v,x}$ and $\phi_{v,y}$, which appear in the vibrational-internal-energy equation are defined by [55]:

$$\phi_{v,x} = \sum_{s=mol}\rho_s v_{sx}h_{v,s}\text{ and }\phi_{v,y} = \sum_{s=mol}\rho_s v_{sy}h_{v,s}\,,$$ (31)

with $h_{v,s}$ being the specific enthalpy (sensible) of the chemical species "s" calculated at the vibrational temperature T_V. The sum of Eq. (14), as also those present in Eq. (31), considers only the molecules of the system, namely: N_2, O_2, NO and NO^+. The θ's terms of Eq. (13) are described as,

$$\theta_{sx} = \left(\mu_m/Sc + \mu_T/Sc_T\right)\partial c_S/\partial x;$$ (32)

$$\theta_{sy} = \left(\mu_m/Sc + \mu_T/Sc_T\right)\partial c_S/\partial y.$$ (33)

The Z total energy is defined as:

$$Z = c_{v,mix}\left(T - T_{REF}\right) + \Delta h_{f,mix}^0 + e_V + 0.5\left(u^2 + v^2\right) + R_b\frac{B^2}{2\rho\mu_M}\,,$$ (34)

with: T_{REF} is the reference temperature, and $\Delta h_{f,mix}^0$ is the mixture formation enthalpy. The pressure term is expressed by:

$$P = p + R_b \frac{B_x^2 + B_y^2}{2\mu_M} = p + R_b \frac{B^2}{2\mu_M}, \tag{35}$$

with p the fluid static pressure. The magnetic force number or pressure number is determined by:

$$R_b = \frac{B_{initial}^2}{\rho_{char} V_{initial}^2 \mu_{M,char}} = \frac{B_{x,initial}^2 + B_{y,initial}^2}{\rho_{char}\left(u_{initial}^2 + v_{initial}^2\right)\mu_{M,char}}, \tag{36}$$

Where $B_{initial}$, $B_{x,initial}$, $B_{y,initial}$, $V_{initial}$, $u_{initial}$, $v_{initial}$, ρ_{char}, and $\mu_{M,char}$ are initial magnetic and flow velocity variables and "char" represents characteristic or freestream flow properties. The laminar Reynolds number is estimated by:

$$Re = \frac{\rho_{char} V_{initial} L_{REF}}{\mu_{m,char}}, \tag{37}$$

with L_{REF} a characteristic configuration length. The magnetic Reynolds number is calculated by:

$$Re_\sigma = L_{REF} V_{initial} \mu_{M,char} \sigma_{char}. \tag{38}$$

The components of the Joule heat flux vector, which characterizes the non-ideal formulation, are determined by:

$$q_{J,x} = -R_b\left\{\frac{B_y}{\mu_M \sigma}\left[\frac{\partial}{\partial x}\left(\frac{B_y}{\mu_M}\right) - \frac{\partial}{\partial y}\left(\frac{B_x}{\mu_M}\right)\right]\right\} \text{ and } q_{J,y} = -R_b\left\{\frac{B_x}{\mu_M \sigma}\left[\frac{\partial}{\partial y}\left(\frac{B_x}{\mu_M}\right) - \frac{\partial}{\partial x}\left(\frac{B_y}{\mu_M}\right)\right]\right\}. \tag{39}$$

5. Turbulence Models

Five turbulence models were implemented according to a k-ω and $k^{1/2}$-ω formulations. Details of the five turbulence models are found in [57, 58]. The interested reader is encouraged to read these references to become aware of the numerical implementation of such models.

6. Centered Scheme

For treat the Maxwell equations, the Maciel centered scheme is implemented. It is obtained by arithmetical average between the flux at the left and right states of the interface. Considering the two-dimensional and structured case, the algorithm is divided in three parts, as recommended by [59], each one corresponding to a characteristic flux. The first part takes into account the dynamics part, which considers the Navier-Stokes equations plus the four equations of the turbulence model and the Maxwell equations, the second one takes into account the chemical part, and the third part takes into account the vibrational part. Hence, the discrete-dynamic-convective flux, which solves the dynamic part, is given by Eq. (40).

$$R_{i+1/2,j} = \frac{1}{2}\left[\begin{pmatrix} \rho u \\ \rho u^2 + P - R_b\,B_x^2/\mu_M \\ \rho uv - R_b\,B_x B_y/\mu_M \\ (\rho Z+P)u - R_b\left(\vec{V}\bullet\vec{B}/\mu_M\right)B_x \\ \rho ku \\ \rho\omega u \\ \rho Q_h u \\ \rho Q_s u \\ 0 \\ uB_y - vB_x \end{pmatrix}_L + \begin{pmatrix} \rho u \\ \rho u^2 + P - R_b\,B_x^2/\mu_M \\ \rho uv - R_b\,B_x B_y/\mu_M \\ (\rho Z+P)u - R_b\left(\vec{V}\bullet\vec{B}/\mu_M\right)B_x \\ \rho ku \\ \rho\omega u \\ \rho Q_h u \\ \rho Q_s u \\ 0 \\ uB_y - vB_x \end{pmatrix}_R \right]S_x +$$

$$\frac{1}{2}\left[\begin{pmatrix} \rho v \\ \rho uv - R_b B_x B_y/\mu_M \\ \rho v^2 + P - R_b B_y^2/\mu_M \\ (\rho Z + P)v - R_b(\vec{V}\bullet\vec{B}/\mu_M)B_y \\ \rho k v \\ \rho\omega v \\ \rho Q_h v \\ \rho Q_s v \\ vB_x - uB_y \\ 0 \end{pmatrix}_L + \begin{pmatrix} \rho v \\ \rho uv - R_b B_x B_y/\mu_M \\ \rho v^2 + P - R_b B_y^2/\mu_M \\ (\rho Z + P)v - R_b(\vec{V}\bullet\vec{B}/\mu_M)B_y \\ \rho k v \\ \rho\omega v \\ \rho Q_h v \\ \rho Q_s v \\ vB_x - uB_y \\ 0 \end{pmatrix}_R\right]S_y ; \qquad (40)$$

the discrete-chemical-convective flux is defined by:

$$R_{i+1/2,j} = \frac{1}{2}\left[\begin{pmatrix} \rho_1 u \\ \rho_2 u \\ \rho_4 u \\ \rho_5 u \\ \rho_6 u \\ \rho_7 u \end{pmatrix}_L + \begin{pmatrix} \rho_1 u \\ \rho_2 u \\ \rho_4 u \\ \rho_5 u \\ \rho_6 u \\ \rho_7 u \end{pmatrix}_R\right]S_x + \frac{1}{2}\left[\begin{pmatrix} \rho_1 v \\ \rho_2 v \\ \rho_4 v \\ \rho_5 v \\ \rho_6 v \\ \rho_7 v \end{pmatrix}_L + \begin{pmatrix} \rho_1 v \\ \rho_2 v \\ \rho_4 v \\ \rho_5 v \\ \rho_6 v \\ \rho_7 v \end{pmatrix}_R\right]S_y ; \qquad (41)$$

and the discrete-vibrational-convective flux is determined by:

$$R_{i+1/2,j} = \frac{1}{2}\left[(\rho e_v u)_L + (\rho e_v u)_R\right]S_x + \frac{1}{2}\left[(\rho e_v v)_L + (\rho e_v v)_R\right]S_y . \qquad (42)$$

The viscous formulation follows that of [60], which adopts the Green theorem to calculate primitive variable gradients. The viscous gradients at the interface are obtained by arithmetical average between cell (i,j) and its neighbors. As was done with the convective terms, there is a need to separate the viscous flux in three parts: dynamic viscous flux, chemical viscous flux, and vibrational viscous flux. The dynamic part corresponds to the first four equations of the Navier-Stokes ones plus the four equations of the turbulence model plus the two equations of the Maxwell ones, the chemical part corresponds to the six equations immediately below the energy equation, and the vibrational part corresponds to the equation that follows the last chemical one. For the Maciel scheme, the dynamic part is represented by:

$$R_{i+1/2,} = \frac{1}{2}\left[\begin{pmatrix} 0 \\ (t_{xx}+\tau_{xx})/Re \\ (t_{xy}+\tau_{xy})/Re \\ (f_x-\phi_x)/Re - q_{J,x}/Re_\sigma \\ \alpha_x/Re \\ \beta_x/Re \\ \gamma_x/Re \\ \delta_x/Re \\ 0 \\ \frac{1}{Re_\sigma}\frac{1}{\sigma}\left[\frac{\partial}{\partial x}\left(\frac{B_y}{\mu_M}\right) - \frac{\partial}{\partial y}\left(\frac{B_x}{\mu_M}\right)\right] \end{pmatrix}_L + \begin{pmatrix} 0 \\ (t_{xx}+\tau_{xx})/Re \\ (t_{xy}+\tau_{xy})/Re \\ (f_x-\phi_x)/Re - q_{J,x}/Re_\sigma \\ \alpha_x/Re \\ \beta_x/Re \\ \gamma_x/Re \\ \delta_x/Re \\ 0 \\ \frac{1}{Re_\sigma}\frac{1}{\sigma}\left[\frac{\partial}{\partial x}\left(\frac{B_y}{\mu_M}\right) - \frac{\partial}{\partial y}\left(\frac{B_x}{\mu_M}\right)\right] \end{pmatrix}_R\right]S_x +$$

$$\frac{1}{2}\left[\begin{pmatrix} 0 \\ (t_{xy}+\tau_{xy})/Re \\ (t_{yy}+\tau_{yy})/Re \\ (f_y-\phi_y)/Re - q_{J,y}/Re_\sigma \\ \alpha_y/Re \\ \beta_y/Re \\ \gamma_y/Re \\ \delta_y/Re \\ \dfrac{1}{Re_\sigma}\dfrac{1}{\sigma}\left[\dfrac{\partial}{\partial y}\left(\dfrac{B_x}{\mu_M}\right)-\dfrac{\partial}{\partial x}\left(\dfrac{B_y}{\mu_M}\right)\right] \\ 0 \end{pmatrix}_L + \begin{pmatrix} 0 \\ (t_{xy}+\tau_{xy})/Re \\ (t_{yy}+\tau_{yy})/Re \\ (f_y-\phi_y)/Re - q_{J,y}/Re_\sigma \\ \alpha_y/Re \\ \beta_y/Re \\ \gamma_y/Re \\ \delta_y/Re \\ \dfrac{1}{Re_\sigma}\dfrac{1}{\sigma}\left[\dfrac{\partial}{\partial y}\left(\dfrac{B_x}{\mu_M}\right)-\dfrac{\partial}{\partial x}\left(\dfrac{B_y}{\mu_M}\right)\right] \\ 0 \end{pmatrix}_R\right]S_y; \tag{43}$$

To the chemical part one has:

$$R_{i+1/2,j} = \frac{1}{2}\left[\begin{pmatrix} (-\rho_1 v_{1x}-\theta_{1x})/Re \\ (-\rho_2 v_{2x}-\theta_{2x})/Re \\ (-\rho_4 v_{4x}-\theta_{4x})/Re \\ (-\rho_5 v_{5x}-\theta_{5x})/Re \\ (-\rho_6 v_{6x}-\theta_{6x})/Re \\ (-\rho_7 v_{7x}-\theta_{7x})/Re \end{pmatrix}_L + \begin{pmatrix} (-\rho_1 v_{1x}-\theta_{1x})/Re \\ (-\rho_2 v_{2x}-\theta_{2x})/Re \\ (-\rho_4 v_{4x}-\theta_{4x})/Re \\ (-\rho_5 v_{5x}-\theta_{5x})/Re \\ (-\rho_6 v_{6x}-\theta_{6x})/Re \\ (-\rho_7 v_{7x}-\theta_{7x})/Re \end{pmatrix}_R\right]S_x +$$

$$\frac{1}{2}\left[\begin{pmatrix} (-\rho_1 v_{1y}-\theta_{1y})/Re \\ (-\rho_2 v_{2y}-\theta_{2y})/Re \\ (-\rho_4 v_{4y}-\theta_{4y})/Re \\ (-\rho_5 v_{5y}-\theta_{5y})/Re \\ (-\rho_6 v_{6y}-\theta_{6y})/Re \\ (-\rho_7 v_{7y}-\theta_{7y})/Re \end{pmatrix}_L + \begin{pmatrix} (-\rho_1 v_{1y}-\theta_{1y})/Re \\ (-\rho_2 v_{2y}-\theta_{2y})/Re \\ (-\rho_4 v_{4y}-\theta_{4y})/Re \\ (-\rho_5 v_{5y}-\theta_{5y})/Re \\ (-\rho_6 v_{6y}-\theta_{6y})/Re \\ (-\rho_7 v_{7y}-\theta_{7y})/Re \end{pmatrix}_R\right]S_y; \tag{44}$$

Finally, to the vibrational part:

$$R_{i+1/2,j} = \frac{1}{2}\left[\left(\frac{q_{v,x}-\phi_{v,x}}{Re}\right)_L + \left(\frac{q_{v,x}-\phi_{v,x}}{Re}\right)_R\right]S_x + \frac{1}{2}\left[\left(\frac{q_{v,y}-\phi_{v,y}}{Re}\right)_L + \left(\frac{q_{v,y}-\phi_{v,y}}{Re}\right)_R\right]S_y. \tag{45}$$

where $S_{i+1/2,j} = \begin{bmatrix} S_x & S_y \end{bmatrix}^t_{i+1/2,j}$ defines the normal area vector for the surface (i+½,j). The normal area components S_x and S_y to each flux interface are given in Tab. 1. Figure 1 exhibits the computational cell adopted for the simulations, as well its respective nodes and flux interfaces.

The resultant ordinary differential equation system can be written as:

$$V_{i,j}\,dQ_{i,j}/dt = -(R_{i,j-1/2} + R_{i+1/2,j} + R_{i,j+1/2} + R_{i-1/2,j}) = -C_{i,j}, \tag{46}$$

where the cell volume is given by:

$$V_{i,j} = 0.5\left|(x_{i,j}-x_{i+1,j})y_{i+1,j+1} + (x_{i+1,j}-x_{i+1,j+1})y_{i,j} + (x_{i+1,j+1}-x_{i,j})y_{i+1,j}\right| +$$

$$0.5\left|(x_{i,j}-x_{i+1,j+1})y_{i,j+1} + (x_{i+1,j+1}-x_{i,j+1})y_{i,j} + (x_{i,j+1}-x_{i,j})y_{i+1,j+1}\right|. \tag{47}$$

Journal of Scientific and Engineering Research

This centered scheme needs an artificial dissipation operator, D, to guarantee stability in presence of shock waves and background instabilities. Considering this operator, Eq. (46) can be rewritten as:

$$dQ_{i,j}/dt = -\left(C_{i,j} - D_{i,j}\right)/V_{i,j} , \qquad (48)$$

where D has the following structure:

$$D\left(Q_{i,j}\right) = d^{(2)}\left(Q_{i,j}\right) - d^{(4)}\left(Q_{i,j}\right), \qquad (49)$$

with:

$$d^{(2)} = 0.5\varepsilon^{(2)}_{i,j-1/2}\left(A_{i,j} + A_{i,j-1}\right)\left(Q_{i,j-1} - Q_{i,j}\right) + 0.5\varepsilon^{(2)}_{i+1/2,j}\left(A_{i,j} + A_{i+1,j}\right)\left(Q_{i+1,j} - Q_{i,j}\right) +$$
$$0.5\varepsilon^{(2)}_{i,j+1/2}\left(A_{i,j} + A_{i,j+1}\right)\left(Q_{i,j+1} - Q_{i,j}\right) + 0.5\varepsilon^{(2)}_{i-1/2,j}\left(A_{i,j} + A_{i-1,j}\right)\left(Q_{i-1,j} - Q_{i,j}\right) \qquad (50)$$

named the undivided Laplacian operator, responsible by the numerical stability in presence of shock waves; and

$$d^{(4)} = 0.5\varepsilon^{(4)}_{i,j-1/2}\left(A_{i,j} + A_{i,j-1}\right)\left(\nabla^2 Q_{i,j-1} - \nabla^2 Q_{i,j}\right) +$$
$$0.5\varepsilon^{(4)}_{i+1/2,j}\left(A_{i,j} + A_{i+1,j}\right)\left(\nabla^2 Q_{i+1,j} - \nabla^2 Q_{i,j}\right) +$$
$$0.5\varepsilon^{(4)}_{i,j+1/2}\left(A_{i,j} + A_{i,j+1}\right)\left(\nabla^2 Q_{i,j+1} - \nabla^2 Q_{i,j}\right) +$$
$$0.5\varepsilon^{(4)}_{i-1/2,j}\left(A_{i,j} + A_{i-1,j}\right)\left(\nabla^2 Q_{i-1,j} - \nabla^2 Q_{i,j}\right), \qquad (51)$$

named the bi-harmonic operator, responsible by the background stability (odd-even instabilities, for instance). In this last term,

$$\nabla^2 Q_{i,j} = \left(Q_{i,j-1} - Q_{i,j}\right) + \left(Q_{i+1,j} - Q_{i,j}\right) + \left(Q_{i,j+1} - Q_{i,j}\right) + \left(Q_{i-1,j} - Q_{i,j}\right). \qquad (52)$$

In the $d^{(4)}$ operator, $\nabla^2 Q_{i,j}$ is extrapolated from your neighbor cell every time that such one represents an especial boundary layer cell, recognized in the CFD literature as "ghost" cell. The ε terms are defined, for instance, as:

$$\varepsilon^{(2)}_{i,j-1/2} = K^{(2)}MAX\left(\nu_{i,j}, \nu_{i,j-1}\right) \text{ and } \varepsilon^{(4)}_{i,j-1/2} = MAX\left[0, \left(K^{(4)} - \varepsilon^{(2)}_{i,j-1/2}\right)\right], \qquad (53)$$

in which:

$$\nu_{i,j} = \left(\left|p_{i,j-1} - p_{i,j}\right| + \left|p_{i+1,j} - p_{i,j}\right| + \left|p_{i,j+1} - p_{i,j}\right| + \left|p_{i-1,j} - p_{i,j}\right|\right)/\left(p_{i,j-1} + p_{i+1,j} + p_{i,j+1} + p_{i-1,j} + 4p_{i,j}\right). \qquad (54)$$

represents a pressure sensor employed to identify regions of high gradients. Each time that a neighbor cell represent a ghost cell, it is assumed that, for instance, $\nu_{ghost} = \nu_{i,j}$. The $A_{i,j}$ terms define the particular artificial dissipation operator. Two models were studied in the current work:

(a)   Artificial dissipation operator of Mavriplis / Scalar, non-linear, and isotropic model:
In this case, the $A_{i,j}$ terms represent the sum of the contributions of the maximum normal eigenvalue associated to the flux interface of the Euler equations, integrated along each cell face. Based on [61] work, these terms are defined as:

$$A_{i,j} = \left[\left|u_{int}S_x + v_{int}S_y\right|_{i,j-1/2} + a_{int}\left(S_x^2 + S_y^2\right)^{0.5}_{i,j-1/2}\right] + \left[\left|u_{int}S_x + v_{int}S_y\right|_{i+1/2,j} + a_{int}\left(S_x^2 + S_y^2\right)^{0.5}_{i+1/2,j}\right] +$$
$$\left[\left|u_{int}S_x + v_{int}S_y\right|_{i,j+1/2} + a_{int}\left(S_x^2 + S_y^2\right)^{0.5}_{i,j+1/2}\right] + \left[\left|u_{int}S_x + v_{int}S_y\right|_{i-1/2,j} + a_{int}\left(S_x^2 + S_y^2\right)^{0.5}_{i-1/2,j}\right], \qquad (55)$$

where "a" represents the sound speed and the interface properties are evaluated by arithmetical average. The $K^{(2)}$ and $K^{(4)}$ constants have typical values of 1/4 and 3/256, respectively.

(b)   Artificial dissipation model of Turkel and Vatsa / Scalar, non-linear, and anisotropic model:
The aforementioned artificial dissipation model presents the characteristic of being isotropic. In words, the dissipation introduced artificially in a given coordinate direction to stabilize the scheme weights equally the phenomena originated from all directions, having not a more significant weighting from the particular direction under study. The dissipation is clearly isotropic. The scalar, non-linear and anisotropic artificial dissipation model of [62] aims to provide a numerical attenuation that considers with bigger weight the propagation

information effects associated to the characteristic maximum eigenvalue from the coordinate direction under study. Basically, such artificial dissipation model differs from the non-linear, isotropic model of [61] only in the determination of the weighting term of the dissipation operator.

$$A_\xi = \overline{\lambda}_{\xi_{i+1/2,j}} \left[1 + \left(\overline{\lambda}_\eta \Big/ \overline{\lambda}_\xi \right)_{i+1/2,j}^{0.5} \right], \ \overline{\lambda}_{\xi_{i+1/2,j}} = \left(\left| un_x + vn_y \right| + a \right)_{i+1/2,j} S_{i+1/2,j} \ \text{and}$$

$$\overline{\lambda}_{\eta_{i+1/2,j}} = \left(\left| un_x + vn_y \right| + a \right)_{i+1/2,j} S_{i+1/2,j}; \tag{56}$$

$$A_\eta = \overline{\lambda}_{\eta_{i,j+1/2}} \left[1 + \left(\overline{\lambda}_\xi \Big/ \overline{\lambda}_\eta \right)_{i,j+1/2}^{0.5} \right], \ \overline{\lambda}_{\xi_{i,j+1/2}} = \left(\left| un_x + vn_y \right| + a \right)_{i,j+1/2} S_{i,j+1/2} \ \text{and}$$

$$\overline{\lambda}_{\eta_{i,j+1/2}} = \left(\left| un_x + vn_y \right| + a \right)_{i,j+1/2} S_{i,j+1/2}. \tag{57}$$

To this artificial dissipation model, the recommended values of $K^{(2)}$ and $K^{(4)}$ by [44] are 1/2 and 1/64, respectively.

In the present study, the Euler backward method was employed to march the scheme in time. This method is first-order accurate in time, to the three types of complete flux. To the convective dynamic component, this method can be represented in general form by:

$$Q_{i,j}^{(n+1)} = Q_{i,j}^{(n)} - \left(\Delta t_{i,j} / V_{i,j} \right) \times \left[C\left(Q_{i,j}^{(n)}\right) - D\left(Q_{i,j}^{(n)}\right) \right], \tag{58}$$

to the convective chemical component, it can be represented in general form by:

$$Q_{i,j}^{(n+1)} = Q_{i,j}^{(n)} - \Delta t_{i,j} \times \left\{ \left[C\left(Q_{i,j}^{(n)}\right) - D\left(Q_{i,j}^{(n)}\right) \right] / V_{i,j} - S_C\left(Q_{i,j}^{(n)}\right) \right\}, \tag{59}$$

where the chemical source term S_C is calculated with the temperature T_{rrc} (reaction rate controlling temperature, see [51-52]). Finally, to the convective vibrational component:

$$Q_{i,j}^{(n+1)} = Q_{i,j}^{(n)} - \Delta t_{i,j} \times \left\{ \left[C\left(Q_{i,j}^{(n)}\right) - D\left(Q_{i,j}^{(n)}\right) \right] / V_{i,j} - S_V\left(Q_{i,j}^{(n)}\right) \right\}, \tag{60}$$

in which:

$$S_V = \sum_{s=mol} q_{T-V,s} + \sum_{s=mol} S_{C,s} e_{v,s}, \tag{61}$$

where q_{T-V} is the heat flux due to translational-vibrational relaxation, defined in Eq. (14) and in [51-52].

7. Spatially Variable Time Step
The spatially variable time step has proved efficient gains in terms of convergence acceleration, as verified by [42-43]. Initially, the parameter σ is determined, where:

$$\sigma_s = \frac{c_s}{M_s} \ \text{and} \ \sigma = \sum_{s=1}^{ns} \sigma_s, \tag{62}$$

with c_s being the mass fraction and M_s the molecular weight. The total specific heat at constant volume due to translation is defined as:

$$c_{V,T} = \sum_{s=1}^{ns} \sigma_s c_{V,T,s}, \tag{63}$$

where, for each gas constituent of the seven (7) species chemical model, the specific heat at constant volume, based on the kinetic theory of gases [63], is defined by

$$c_{V,T,N} = \frac{3}{2} R_N, \ c_{V,T,O} = \frac{3}{2} R_O, \ c_{V,T,N_2} = \frac{5}{2} R_{N_2}, \ c_{V,T,O_2} = \frac{5}{2} R_{O_2}, \ c_{V,T,NO} = \frac{5}{2} R_{NO};$$

$$c_{V,T,NO^+} = \frac{5}{2} R_{NO^+} \ \text{and} \ c_{V,T,e^-} = \frac{3}{2} R_{e^-}. \tag{64}$$

being R_s the specific gas constant. The total pressure of the gaseous mixture is determined by Dalton law, which indicates that the total pressure of the gas is the sum of the partial pressure of each constituent gas, resulting in:

$$p_s = c_s \rho R_s T \text{ and } p = \sum_{s=1}^{ns} p_s . \tag{65}$$

The speed of sound to a reactive mixture considering the two-equation turbulence models can be determined by

$$a = \sqrt{(\beta + 1)\frac{p}{\rho} - k}, \tag{66}$$

where $\beta = \dfrac{R_{univ}\sigma}{c_{V,T}}$, with R_{univ} = 1.987 cal/(g-mol.K). Finally, the spatially variable time step is defined from the CFL (Courant, Friedrichs, and Lewis) definition:

$$\Delta t_{i,j} = \frac{CFL \Delta s_{i,j}}{\sqrt{u_{i,j}^2 + v_{i,j}^2 + a_{i,j}}}, \tag{67}$$

with $\Delta s_{i,j}$ is the characteristic length of each cell (defined between the minimum cell side length and the minimum centroid distance between each cell and its neighbors).

8. Dimensionless Scales, Initial and Boundary Conditions
8.1. Dimensionless Scales
The dimensionless scales employed to the reactive equations consisted in: R_s is dimensionless by a_{char}, where $a_{char} = \sqrt{\gamma p_{char}/\rho_{char}}$; c_v is dimensionless by a_{char}; h_s and Δh_s^0 are dimensionless by a_{char}^2; T and T_v, translational/rotational temperature and vibrational temperature, respectively, are dimensionless by a_{char}; ρ_s and ρ are dimensionless by ρ_{char}; u and v are dimensionless by a_{char}; μ_m is dimensionless by $\mu_{m,char}$; D, diffusion coefficient, dimensionless by $a_{char}^2 dt_{char}$, where dt_{char} is the minimum time step calculated in the computational domain at the first iteration; $\dot{\omega}$ is dimensionless by $(\rho_{char}/dt_{char})x10^{-3}$; e_v is dimensionless by a_{char}^2; e and p are dimensionless by $\rho_{char}a_{char}^2$; τ_s, relaxation time, is dimensionless by dt_{char}. To the Maxwell equations: the B_x and B_y Cartesian components of the magnetic field dimensionless by $B_{initial}$; the magnetic permeability of the mean is dimensionless by $\mu_{M,char}$; and the electric conductivity is dimensionless by σ_{char}. The characteristic parameters are defined in [64].

8.2. Initial Condition
The initial conditions to the blunt body problem, for a seven species chemical model, are presented in Tab. 2. The Reynolds number is obtained from data of [64].

8.3. Boundary Conditions
The boundary conditions are basically of three types: solid wall, entrance, and exit. These conditions are implemented with the help of ghost cells.

Wall condition
To the viscous case, the boundary condition imposes that the ghost cell velocity components be equal to the real cell velocity components, with the negative signal:

$$u_g = -u_r \text{ and } v_g = -v_r . \tag{68}$$

The normal pressure gradient of the fluid at the wall is assumed to be equal to zero according to a boundary-layer like condition. The same hypothesis is applied for the normal temperature gradient at the wall, assuming an adiabatic wall. From the above considerations, density and translational/rotational temperature are

extrapolated from the respective values of its real neighbor volume (zero order extrapolation). The total vibrational internal energy is also extrapolated. With the mixture species mass fractions and with the values of the respective specific heats at constant volume, it is possible to obtain the mixture specific heat at constant volume. The mixture formation enthalpy is extrapolated from the real cell.

For the turbulent case, the turbulent kinetic energy and the turbulent vorticity at the ghost volumes are determined by the following expressions:

$$k_{ghost} = 0.0 \text{ and } \omega^2_{ghost} = \left[(38/3\nu_M)/(\beta d_n^2) \right]^2, \tag{69}$$

where β assumes the value 3/40 and d_n is the distance of the first cell to the wall. The Q_h and Q_s variables are fixed by their initial values.

For the magnetic case, the Cartesian components of the induced magnetic field at the wall to the ghost cells are fixed with their initial values. The magnetic permeability is considered constant with its initial value. The mixture total energy to the ghost cell is calculated by:

$$Z_g = c_{v\,mixt,g}\left(T_{tr,g} - T_{REF}\right) + \Delta h^0_{mixt,g} + e_{v,nond\,g} + 0.5\left(u_g^2 + v_g^2\right) + R_b\left(B_{x,g}^2 + B_{y,g}^2\right)/\left(2\mu_{M,g}\rho_g\right). \tag{70}$$

Entrance condition

It is divided in two flow regimes:

(a) Subsonic flow: Seven properties are specified and three extrapolated in the boundary conditions of the dynamic part of the Maciel algorithm. This approach is based on information propagation analysis along characteristic directions in the calculation domain ([65]). In other words, for subsonic flow, seven characteristics propagate information pointing into the computational domain. Thus seven flow properties must be fixed at the inlet plane. Just three characteristic lines allow information to travel upstream. So, three flow variables must be extrapolated from the interior grid to the inlet boundary. The total energy and the components of the magnetic field were the extrapolated variables from the real neighbor volumes, for the studied problems. Density and velocity components adopted values of initial flow. The turbulence kinetic energy and the vorticity were fixed with the values of the initial condition. Q_h and Q_s variables are also fixed with the values $10^{-6} h^2_{initial}$ and 10^{-3} $\sum_{i=1}^{ns} c^2_{i,initial}$, respectively. To the chemical part, six information propagate upstream because it is assumed that all six equations are conducted by the eigenvalue "(q_n-a)". In the subsonic flow, all eigenvalues are negative and the information should be extrapolated. In the same reasoning to the chemical boundary conditions, the vibrational-internal-energy equation is dictated by the "(q_n-a)" eigenvalue and, in the subsonic region, its value is negative. Hence, the vibrational internal energy should be extrapolated.

(b) Supersonic flow: In this case no information travels upstream; therefore all variables are fixed with their initial values.

Exit condition

It is also divided in two flow regimes:

(a) Subsonic flow: Three characteristics propagate information outward the computational domain. Hence, the associated variables should be extrapolated from interior information. The characteristic direction associated to the "$(q_{normal}-a)$" velocity should be specified because it points inward to the computational domain [65]. In this case, the ghost volume total energy and the induced magnetic components are specified from their initial value. Density and velocity components are extrapolated. The turbulence kinetic energy and the vorticity are prescribed and receive the following values: $0.01k_{ff}$ and $10u/L_{REF}$, respectively, where $k_{ff} = 0.5u^2$. For the [28] model, consider the squared root of $0.01k_{ff}$. Q_h and Q_s variables are also fixed with the values $10^{-6} h^2_{initial}$ and $10^{-3} \sum_{i=1}^{ns} c^2_{i,initial}$, respectively. To the chemical part, the eigenvalue "(q_n-a)" is again negative and the characteristics are always flowing in to the computational domain. Hence, the six chemical species under study should have

their densities fixed by their initial values. In the same reasoning, the internal vibrational energy should have its value prescribed by its initial value due to the eigenvalue "(q_n-a)" be negative.

(b) Supersonic flow: All variables are extrapolated from interior grid cells, as no flow information can make its way upstream. In other words, nothing can be fixed.

9. Physical Problem

One physical problem was solved in this work, namely: the blunt body problem. For this problem, the geometry is a blunt body with 1.0 m of nose ratio and parallel rectilinear walls. The far field is located at 20.0 times the nose ratio in relation to the configuration nose. A mesh composed of 2,548 rectangular cells and 2,650 nodes, with an exponential stretching of 5.0%, was studied. This mesh is equivalent in finite differences to a one of 53x50 points. Figure 2 show the detail of the geometry and Fig. 3 exhibit the viscous mesh.

10. Results

Tests were performed in a Core i7 processor of 2.1GHz and 6.0Gbytes of RAM microcomputer, in a Windows 7.0 environment. Three (3) orders of reduction of the maximum residual in the field were considered to obtain a converged solution. The residual was defined as the value of the discretized conservation equation. In the dynamic part of the Maciel scheme, such definition results in:

$$\text{Re sidual} \quad = \quad -\Delta t_{i,j}/V_{i,j} \times \left(C_{i,j} - D_{i,j} \right). \tag{71}$$

The attack angle was adopted equal to zero. Only the [61] artificial dissipation operator has yielded converged results. In this work, the blunt body turbulent results were obtained for a 16th order of accuracy of the spectral method. For a matter of simplicity, the following abbreviations were used: Maciel scheme = MAC, [28] model = C83, [29] model = W88, [30] model = YGO96, [31] model = C97, [32] model = RGYB98, Chebyshev-Gauss-Radau = CGR, Chebyshev-Gauss-Lobatto = CGL, Legendre-Gauss-Radau = LGR, and Legendre-Gauss-Lobatto = LGL.

10.1. Coakley (1983) Results

Figures 4 to 7 exhibit the pressure contours, the translational/rotational temperature contours, the B_x component of the magnetic field, and the NO mass fraction contours, respectively, obtained by the MAC scheme as using the C83 turbulence model and CGR collocation points. Figures 8 to 11 show the pressure contours, the translational/rotational temperature contours, the B_x component of the magnetic field, and the NO mass fraction contours, respectively, obtained by the MAC scheme as using the C83 turbulence model and the CGL collocation points. Figures 12 to 15 present the pressure contours, the translational/rotational temperature contours, the B_x component of the magnetic field, and the NO mass fraction contours, respectively, obtained by the MAC scheme as using the C83 turbulence model and the LGR collocation points. Finally, Figures 16 to 19 exhibit the pressure contours, the translational/rotational temperature contours, the B_x component of the magnetic field, and the NO mass fraction contours, respectively, obtained by the MAC scheme as using the C83 turbulence model and the LGL collocation points. Good symmetry properties are observed in all these contours. The shock wave is well captured by the MAC scheme. The maximum pressure in the field is obtained when using the CGR collocation points. The symmetric behavior of the B_x component of the magnetic field is verified in these figures. Good formation of NO is also captured by the numerical scheme solution. Good homogeneous properties are observed in all figures. The maximum temperature in the field is obtained by the LGL collocation points and has the value of 21,247.20K.

10.2. Wilcox (1988) Results

Figures 20 to 23 exhibit the pressure contours, the translational/rotational temperature contours, the B_x component of the magnetic field, and the NO mass fraction contours, respectively, obtained by the MAC scheme as using the W88 turbulence model and CGR collocation points. Figures 24 to 27 show the pressure contours, the translational/rotational temperature contours, the B_x component of the magnetic field, and the NO mass fraction contours, respectively, obtained by the MAC scheme as using the W88 turbulence model and the CGL collocation points. Figures 28 to 31 present the pressure contours, the translational/rotational temperature

contours, the B_x component of the magnetic field, and the NO mass fraction contours, respectively, obtained by the MAC scheme as using the W88 turbulence model and the LGR collocation points. Finally, Figures 32 to 35 exhibit the pressure contours, the translational/rotational temperature contours, the B_x component of the magnetic field, and the NO mass fraction contours, respectively, obtained by the MAC scheme as using the W88 turbulence model and the LGL collocation points. Good symmetry properties are observed in all these contours. The maximum pressure in the field is obtained when using the CGR collocation points. The symmetric behavior of the B_x component of the magnetic field is verified in these figures. Good homogeneous properties are observed in all figures. The maximum temperature in the field is obtained by the CGR collocation points and has the value of 23,196.60K.

10.3. Yoder, Geoirgiadids and Orkwis (1996) Results

Figures 36 to 39 exhibit the pressure contours, the translational/rotational temperature contours, the B_x component of the magnetic field, and the NO mass fraction contours, respectively, obtained by the MAC scheme as using the YGO96 turbulence model and CGR collocation points. Figures 40 to 43 show the pressure contours, the translational/rotational temperature contours, the B_x component of the magnetic field, and the NO mass fraction contours, respectively, obtained by the MAC scheme as using the YGO96 turbulence model and the CGL collocation points. Figures 44 to 47 present the pressure contours, the translational/rotational temperature contours, the B_x component of the magnetic field, and the NO mass fraction contours, respectively, obtained by the MAC scheme as using the YGO96 turbulence model and the LGR collocation points. Finally, Figures 48 to 51 exhibit the pressure contours, the translational/rotational temperature contours, the B_x component of the magnetic field, and the NO mass fraction contours, respectively, obtained by the MAC scheme as using the YGO96 turbulence model and the LGL collocation points. The shock wave is well captured by the MAC scheme. The symmetric behavior of the B_x component of the magnetic field is verified in these figures. Good formation of NO is also captured by the numerical scheme solution. Good homogenous properties are observed in all figures. The maximum temperature in the field is 20,754.60K and is obtained by the LGR collocation points.

10.4. Coakley (1997) Results

Figures 52 to 55 exhibit the pressure contours, the translational/rotational temperature contours, the B_x component of the magnetic field, and the NO mass fraction contours, respectively, obtained by the MAC scheme as using the C97 turbulence model and CGR collocation points. Figures 56 to 59 show the pressure contours, the translational/rotational temperature contours, the B_x component of the magnetic field, and the NO mass fraction contours, respectively, obtained by the MAC scheme as using the C97 turbulence model and the CGL collocation points. Figures 60 to 63 present the pressure contours, the translational/rotational temperature contours, the B_x component of the magnetic field, and the NO mass fraction contours, respectively, obtained by the MAC scheme as using the C97 turbulence model and the LGR collocation points. Finally, Figures 64 to 67 exhibit the pressure contours, the translational/rotational temperature contours, the B_x component of the magnetic field, and the NO mass fraction contours, respectively, obtained by the MAC scheme as using the C97 turbulence model and the LGL collocation points. Good symmetry properties are observed in all these contours. The shock wave is well captured by the MAC scheme. The maximum pressure in the field is obtained when using the CGR collocation points. Good formation of NO is also captured by the numerical scheme solution. The maximum temperature in the field is obtained by the LGL collocation points and has the value of 21,055.50K.

10.5. Rumsey, Gatski, Ying and Bertelrud (1998) Results

Figures 68 to 71 exhibit the pressure contours, the translational/rotational temperature contours, the B_x component of the magnetic field, and the NO mass fraction contours, respectively, obtained by the MAC scheme as using the RGYB98 turbulence model and CGR collocation points. Figures 72 to 75 show the pressure contours, the translational/rotational temperature contours, the B_x component of the magnetic field, and the NO mass fraction contours, respectively, obtained by the MAC scheme as using the RGYB98 turbulence model and

the CGL collocation points. Figures 76 to 79 present the pressure contours, the translational/rotational temperature contours, the B_x component of the magnetic field, and the NO mass fraction contours, respectively, obtained by the MAC scheme as using the RGYB98 turbulence model and the LGR collocation points. Finally, Figures 80 to 83 exhibit the pressure contours, the translational/rotational temperature contours, the B_x component of the magnetic field, and the NO mass fraction contours, respectively, obtained by the MAC scheme as using the RGYB98 turbulence model and the LGL collocation points. Good symmetry properties are observed in all these contours. The maximum pressure in the field is obtained when using the CGR collocation points. The symmetric behavior of the B_x component of the magnetic field is verified in these figures. Good homogenous properties are observed in all figures. The maximum temperature in the field is obtained by LGL collocation points and has the value of 21,821.80K.

10.6. Quantitative Analysis

In order to perform a quantitative analysis, the present reactive results are compared to the perfect gas solutions. The stagnation pressure at the blunt body nose was evaluated assuming the perfect gas formulation. Such parameter calculated at this way is not the best comparison, but in the absence of practical reactive results, this constitutes the best available solution.

To calculate the stagnation pressure at the nose of this configuration, [66] presents in its B Appendix values of the normal shock wave properties ahead of the configuration. The ratio pr_0/pr_∞ is estimated as function of the normal Mach number and the stagnation pressure pr_0 can be determined from this parameter. Hence, Table 3 gives the theoretical stagnation pressure value obtained for the blunt body configuration at the initial-normal-Mach number. The value of pr_∞ is determined by the following expression:

$$pr_\infty = \frac{pr_{initial}}{\rho_{char} \times a_{char}^2}, \tag{72}$$

where, for example, for the blunt body case, $pr_{initial} = 687N/m^2$, $\rho_{char} = 0.004kg/m^3$ and $a_{char} = 317.024m/s$. Considering these values, one concludes that $pr_\infty = 1.709$ (non-dimensional). Using the ratio obtained from [66], the stagnation pressure ahead of the configuration nose is estimated as 170.87 unities. Table 4 compares values of the stagnation pressure obtained from the simulations with the theoretical value and show the percentage errors. As can be seen, the best result is due to the MAC scheme coupled with the C83 turbulence model and using the CGR collocation points, with an error of 1.93%.

As the hypersonic flow along the present configuration was simulated with a zero value to the attack angle, a zero lift coefficient is the expected value for this aerodynamic coefficient. Table 5 exhibits an analysis of the lift aerodynamic coefficient, based only on pressure contribution, in this study. As can be observed, the best estimation of the lift coefficient is due to the MAC scheme coupled with the C83 turbulence model and using the LGR collocation points.

10.7. Computational Performance

Table 6 presents the computational data of the MAC scheme for the blunt body problem. It shows the CFL number and the number of iterations to convergence for all studied cases in the current work. It can be verified that the best performance of the MAC scheme occurred when coupled with the C97 turbulence model and using the LGR collocation points, using a CFL of 0.10 and converging in 1,464 iterations.

As final conclusion, it is possible to highlight that, for the studied problem, the MAC scheme coupled with the C83 turbulence model using CGR collocation points had the best performance in estimating the stagnation pressure, and the lift aerodynamic coefficient was better estimated by the MAC scheme as using the LGR collocation points also coupled with the C83 turbulence model. Moreover, the best performance of the numerical scheme, for the 16th order of accuracy, was coupled with the C97 turbulence model, when using the LGR collocation points, employing a CFL of 0.10, and converging in 1,464 iterations.

Finally, to close this work, the computational cost of the numerical scheme using the several types of collocation points is presented in Tab. 7. For the 16th order of accuracy, the cheapest combination was the MAC scheme coupled with C83 turbulence model and using LGL collocation points with a cost of 0.0019667 sec/per-volume/per-iteration.

Journal of Scientific and Engineering Research

Table 1: Values of S_x and S_y

Surface	S_x	S_y
i,j-1/2	$\left(y_{i+1,j} - y_{i,j}\right)$	$\left(x_{i,j} - x_{i+1,j}\right)$
i+1/2,j	$\left(y_{i+1,j+1} - y_{i+1,j}\right)$	$\left(x_{i+1,j} - x_{i+1,j+1}\right)$
i,j+1/2	$\left(y_{i,j+1} - y_{i+1,j+1}\right)$	$\left(x_{i+1,j+1} - x_{i,j+1}\right)$
i-1/2,j	$\left(y_{i,j} - y_{i,j+1}\right)$	$\left(x_{i,j+1} - x_{i,j}\right)$

Table 2: Initial conditions to the blunt body problem

Property	Value
$M_{initial}$	8.78
$\rho_{initial}$	0.00326 kg/m^3
$pr_{initial}$	687 Pa
$U_{initial}$	4,776 m/s
$T_{initial}$	694 K
$T_{v,initial}$	694 K
Altitude	40,000 m
c_N	10^{-9}
c_O	0.07955
c_{O2}	0.13400
c_{NO}	0.05090
c_{NO+}	0.0
c_{e-}	0.0
L_{REF}	2.0 m
Re_{char}	2.386×10^6
$k_{initial}$	10^{-6}
$\omega_{initial}$	$10 U_{initial}/L_{REF}$
$Q_{h,initial}$	$10^{-4} h_{initial}^2$
$Q_{s,initial}$	$10^{-2} \sum_{i=1}^{ns} c_{i,initial}^2$
$B_{y,initial}$	0.15 T
$\mu_{M,char}$	1.2566×10^{-6} T.m/A
σ_{char}	1,000 ohm/m

Table 3: Values of theoretical stagnation pressure.

Problem:	$M_{initial}$:	pr_0/pr_∞:	pr_∞:	pr_0 (Theoretical):
Blunt body	8.78	99.98	1.709	170.87

Table 4. Values of stagnation pressure and respective errors (16th Order)

Turbulence Model:	Spectral Method:	pr_0: (Numerical)	Error:
Coakley (1983)	Chebyshev-Gauss-Radau	167.58	1.93
	Chebyshev-Gauss-Lobatto	164.85	3.52
	Legendre-Gauss-Radau	142.40	16.66
	Legendre-Gauss-Lobatto	142.60	16.54
Wilcox (1988)	Chebyshev-Gauss-Radau	167.32	2.08
	Chebyshev-Gauss-Lobatto	164.69	3.62

	Legendre-Gauss-Radau	142.13	16.82
	Legendre-Gauss-Lobatto	142.45	16.63
YGO (1996)	Chebyshev-Gauss-Radau	167.15	2.18
	Chebyshev-Gauss-Lobatto	164.58	3.68
	Legendre-Gauss-Radau	141.83	17.00
	Legendre-Gauss-Lobatto	142.03	16.88
Coakley (1997)	Chebyshev-Gauss-Radau	167.22	2.14
	Chebyshev-Gauss-Lobatto	164.79	3.56
	Legendre-Gauss-Radau	141.94	16.91
	Legendre-Gauss-Lobatto	142.29	16.73
RGYB (1998)	Chebyshev-Gauss-Radau	167.29	2.10
	Chebyshev-Gauss-Lobatto	164.74	3.59
	Legendre-Gauss-Radau	142.10	16.84
	Legendre-Gauss-Lobatto	142.57	16.56

Table 5: Values of the lift aerodynamic coefficient (16th Order)

Turbulence Model:	Spectral Method:	c_L:
Coakley (1983)	Chebyshev-Gauss-Radau	2.3058×10^{-14}
	Chebyshev-Gauss-Lobatto	1.5757×10^{-14}
	Legendre-Gauss-Radau	4.1689×10^{-15}
	Legendre-Gauss-Lobatto	5.9560×10^{-15}
Wilcox (1988)	Chebyshev-Gauss-Radau	1.7221×10^{-09}
	Chebyshev-Gauss-Lobatto	7.0407×10^{-10}
	Legendre-Gauss-Radau	3.8422×10^{-10}
	Legendre-Gauss-Lobatto	4.7319×10^{-10}
YGO (1996)	Chebyshev-Gauss-Radau	4.7016×10^{-10}
	Chebyshev-Gauss-Lobatto	3.8543×10^{-10}
	Legendre-Gauss-Radau	1.1315×10^{-10}
	Legendre-Gauss-Lobatto	1.1424×10^{-10}
Coakley (1997)	Chebyshev-Gauss-Radau	1.8384×10^{-11}
	Chebyshev-Gauss-Lobatto	1.7146×10^{-11}
	Legendre-Gauss-Radau	1.0156×10^{-11}
	Legendre-Gauss-Lobatto	1.0055×10^{-11}
RGYB (1998)	Chebyshev-Gauss-Radau	3.9110×10^{-04}
	Chebyshev-Gauss-Lobatto	3.6021×10^{-04}
	Legendre-Gauss-Radau	1.5366×10^{-04}
	Legendre-Gauss-Lobatto	1.4428×10^{-04}

Table 6: Computational data (16h Order)

Turbulence Model:	Spectral Method:	CFL:	Iterations:
Coakley (1983)	Chebyshev-Gauss-Radau	0.06	4,755
	Chebyshev-Gauss-Lobatto	0.04	6,706
	Legendre-Gauss-Radau	0.04	3,670
	Legendre-Gauss-Lobatto	0.04	3,691
Wilcox (1988)	Chebyshev-Gauss-Radau	0.06	4,800
	Chebyshev-Gauss-Lobatto	0.10	2,694
	Legendre-Gauss-Radau	0.06	2,503
	Legendre-Gauss-Lobatto	0.04	3,798
	Chebyshev-Gauss-Radau	0.06	4,786

YGO (1996)	Chebyshev-Gauss-Lobatto	0.08	3,357
	Legendre-Gauss-Radau	0.10	1,482
	Legendre-Gauss-Lobatto	0.10	1,489
Coakley (1997)	Chebyshev-Gauss-Radau	0.06	4,073
	Chebyshev-Gauss-Lobatto	0.06	4,405
	Legendre-Gauss-Radau	0.10	1,464
	Legendre-Gauss-Lobatto	0.06	2,467
RGYB (1998)	Chebyshev-Gauss-Radau	0.06	4,673
	Chebyshev-Gauss-Lobatto	0.08	3,295
	Legendre-Gauss-Radau	0.06	2,455
	Legendre-Gauss-Lobatto	0.02	7,507

Table 7: Computational cost (16th Order)

Turbulence Model:	Spectral Method:	Cost (sec/per-volume/per-iteration)
Coakley (1983)	Chebyshev-Gauss-Radau	0.0020330
	Chebyshev-Gauss-Lobatto	0.0019914
	Legendre-Gauss-Radau	0.0019890
	Legendre-Gauss-Lobatto	0.0019667
Wilcox (1988)	Chebyshev-Gauss-Radau	0.0019874
	Chebyshev-Gauss-Lobatto	0.0019843
	Legendre-Gauss-Radau	0.0019867
	Legendre-Gauss-Lobatto	0.0020078
YGO (1996)	Chebyshev-Gauss-Radau	0.0019678
	Chebyshev-Gauss-Lobatto	0.0019725
	Legendre-Gauss-Radau	0.0019733
	Legendre-Gauss-Lobatto	0.0019780
Coakley (1997)	Chebyshev-Gauss-Radau	0.0019686
	Chebyshev-Gauss-Lobatto	0.0019686
	Legendre-Gauss-Radau	0.0019678
	Legendre-Gauss-Lobatto	0.0019757
RGYB (1998)	Chebyshev-Gauss-Radau	0.0019741
	Chebyshev-Gauss-Lobatto	0.0019725
	Legendre-Gauss-Radau	0.0019772
	Legendre-Gauss-Lobatto	0.0019765
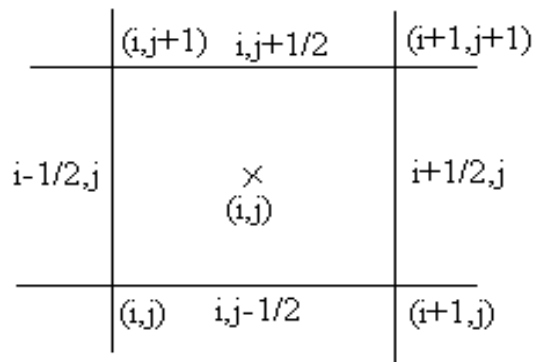
Figure 1: Computational cell
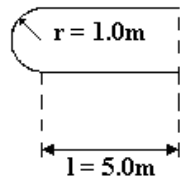
Figure 2: Blunt body geometry
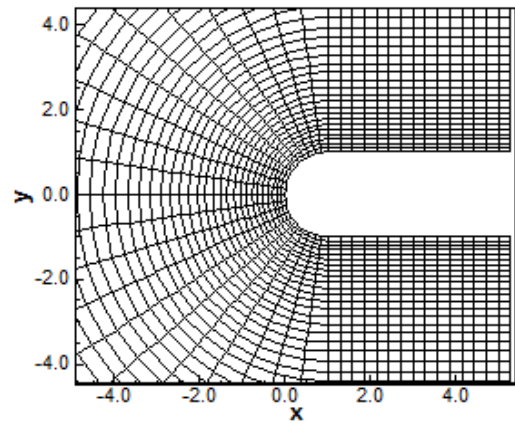
Figure 3: Blunt body viscous mesh

Coakley (1983) Solutions
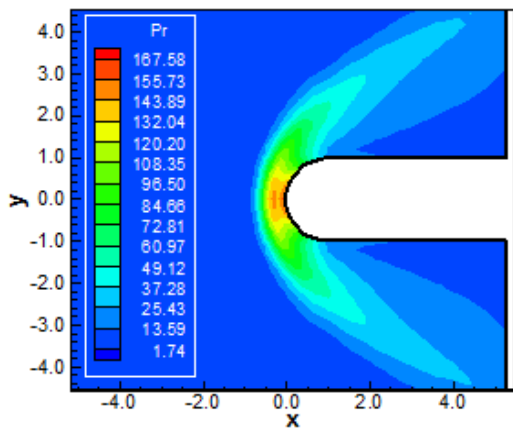
Figure 4: Pressure contours (CGR-C83)
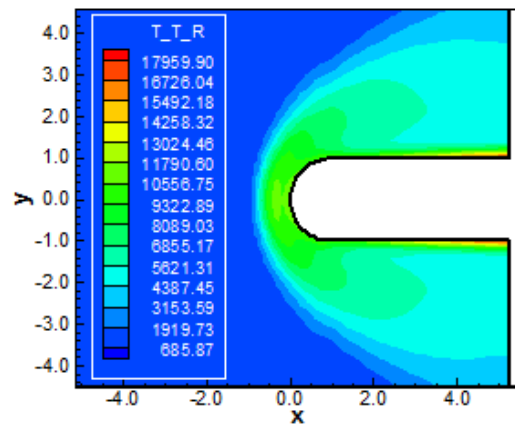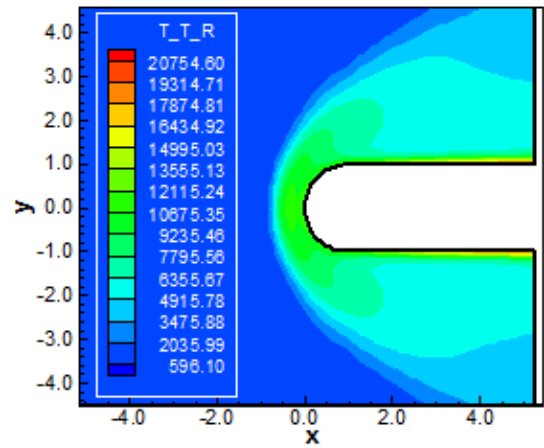

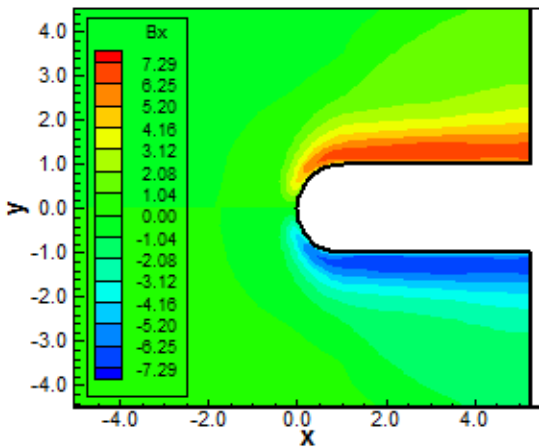Figure 5: Translational/rotational temperature contours (CGR-C83):
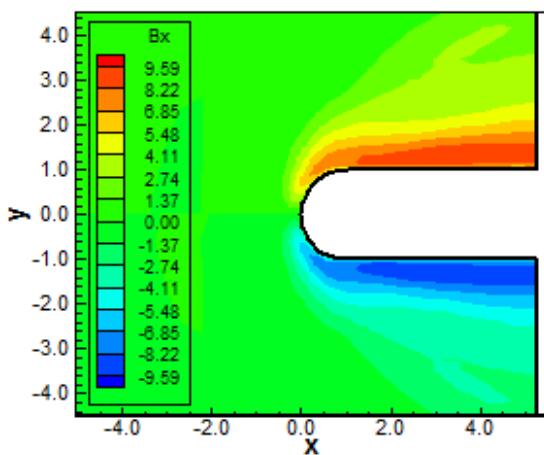
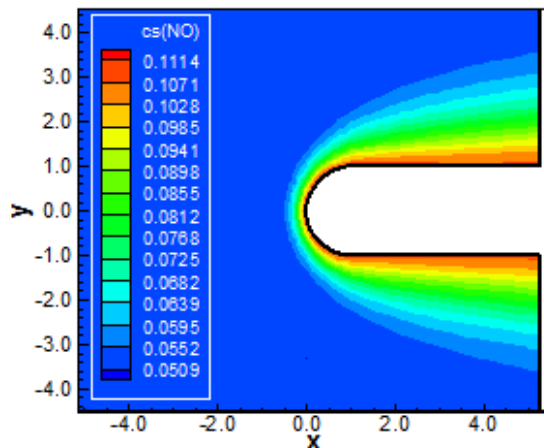Figure 6: B_x component of the magnetic field (CGR-C83)
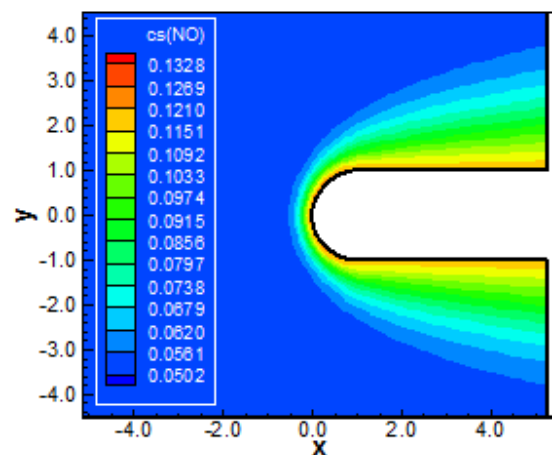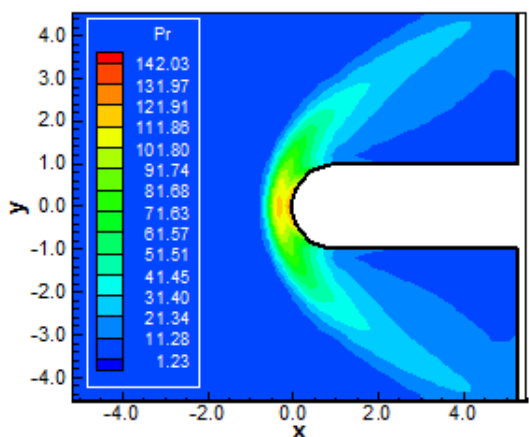

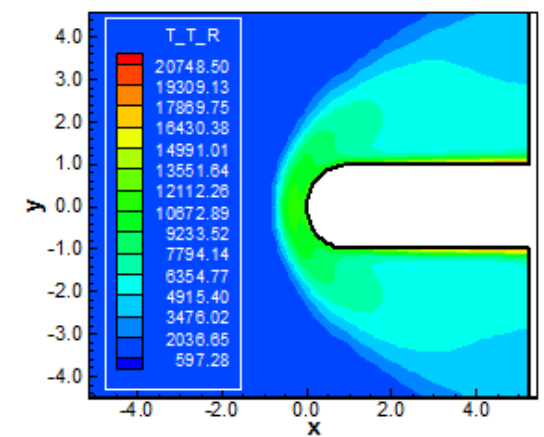Figure 7: NO mass fraction contours (CGR-C83)
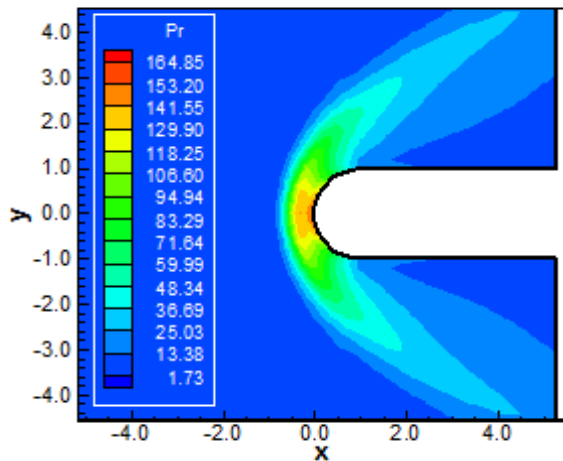
Figure 8: Pressure contours (CGL-C83)
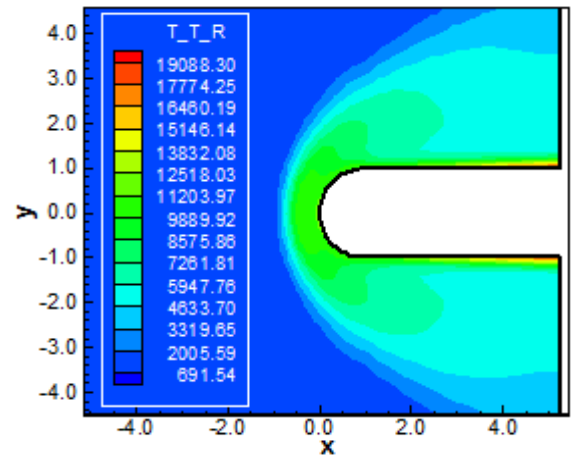
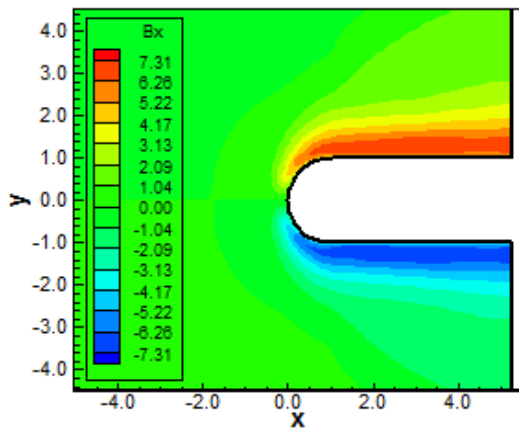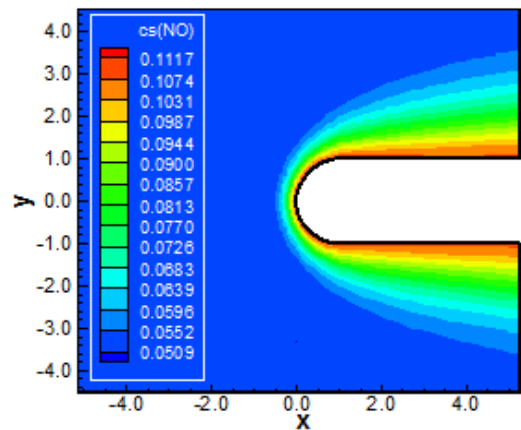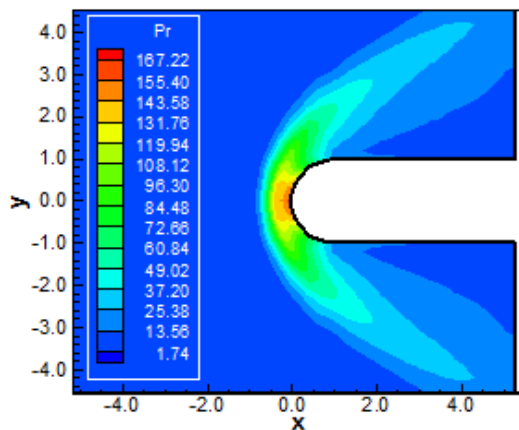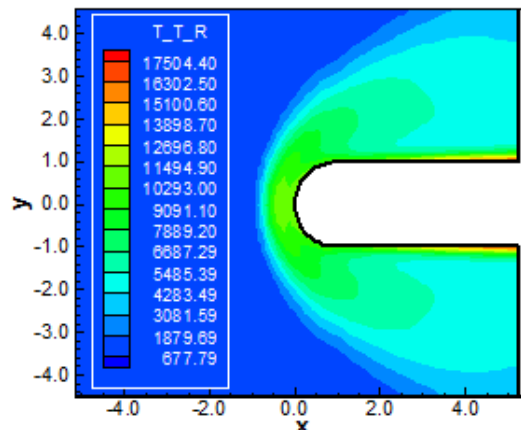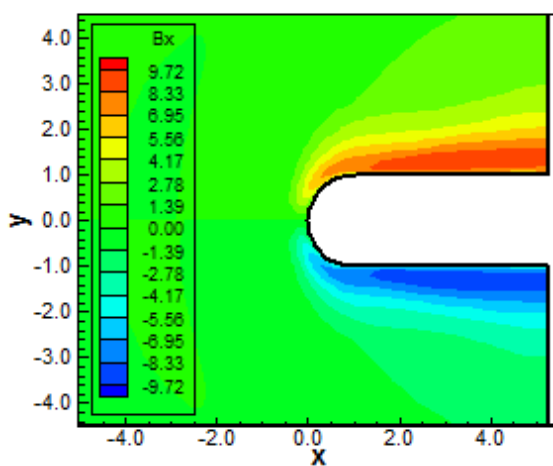*Figure 9: Translational/rotational temperature contours (CGL-C83)*
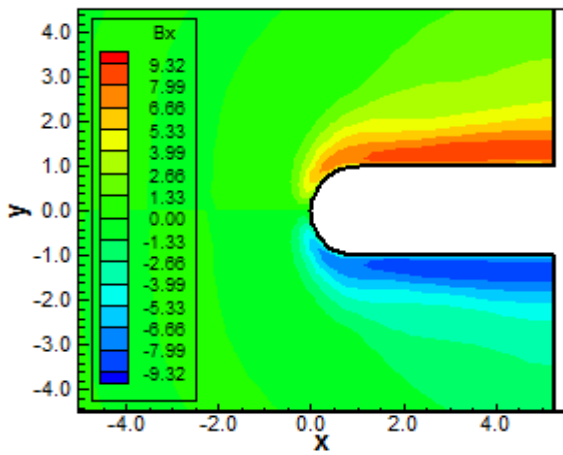
Figure 10: B_x component of the magnetic field (CGL-C83)
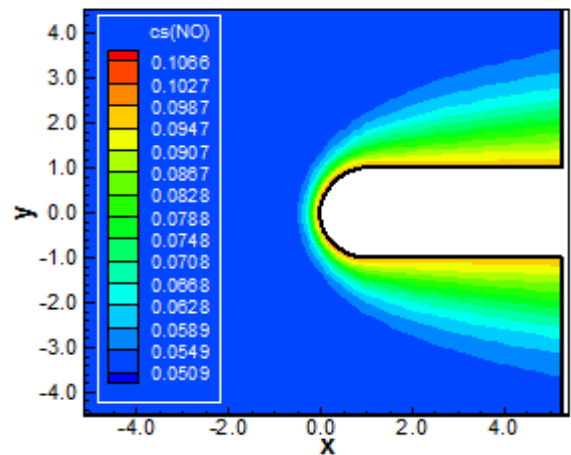
Figure 11: NO mass fraction contours (CGL-C83)
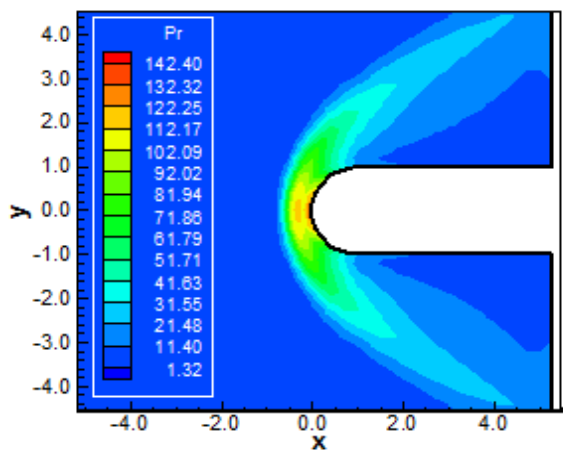
Figure 12: Pressure contours (LGR-C83)
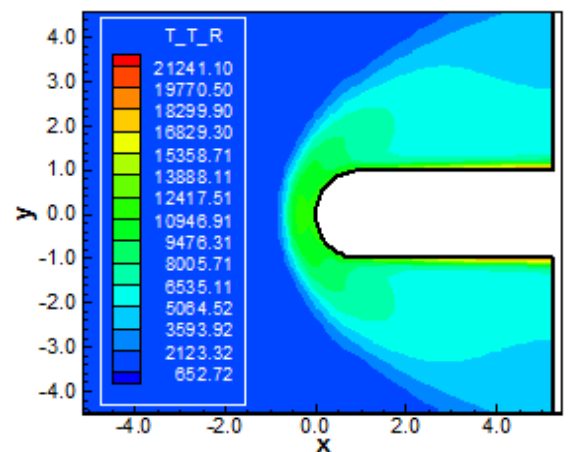
Figure 13: Translational/rotational temperature contours (LGR-C83)
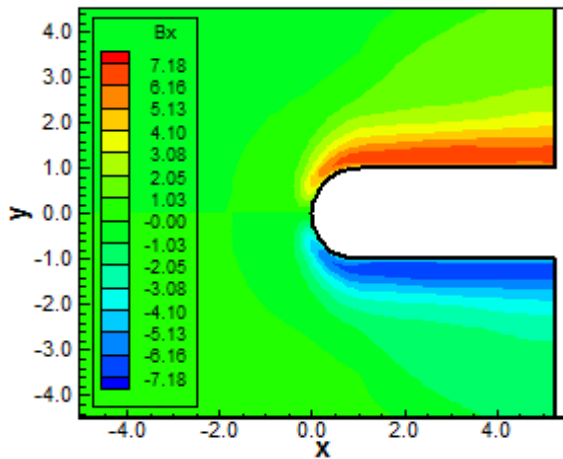
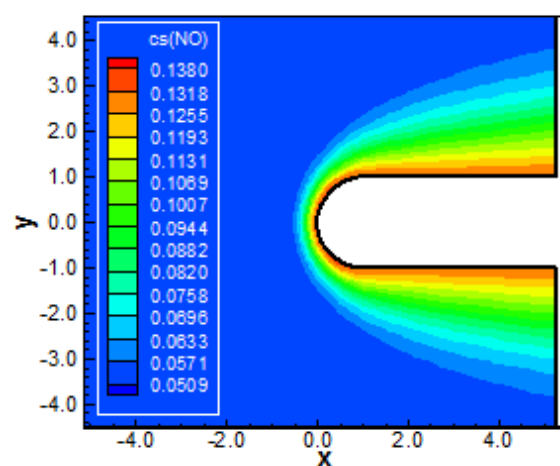*Figure 14: B_x component of the magnetic field (LGR-C83)*
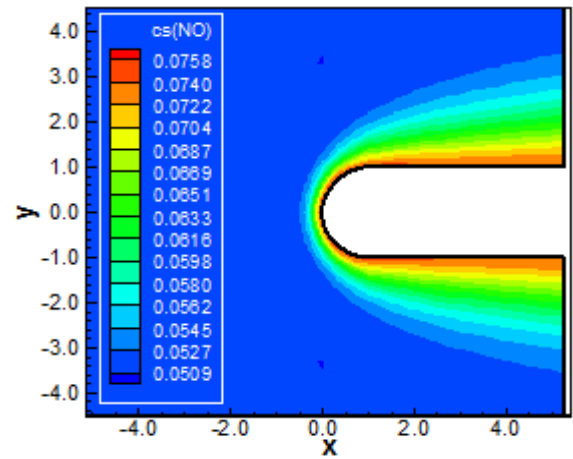
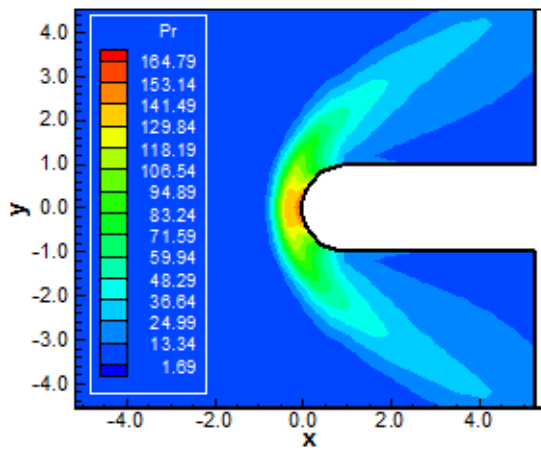*Figure 15: NO mass fraction contours (LGR-C83)*
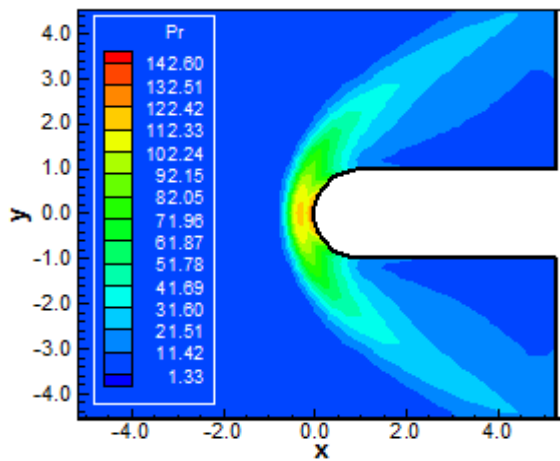
Figure 16: Pressure contours (LGL-C83)
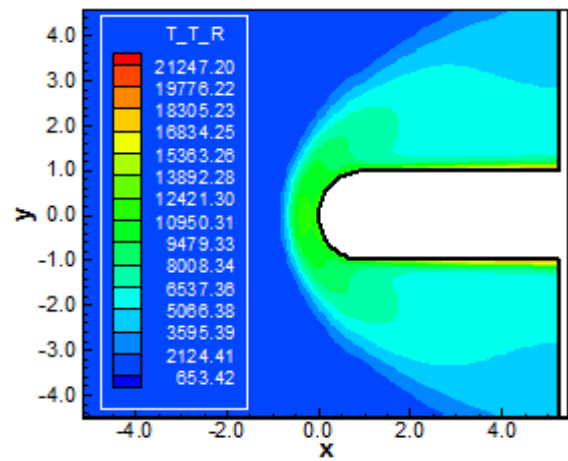
Figure 17: Translational/rotational temperature contours (LGL-C83)
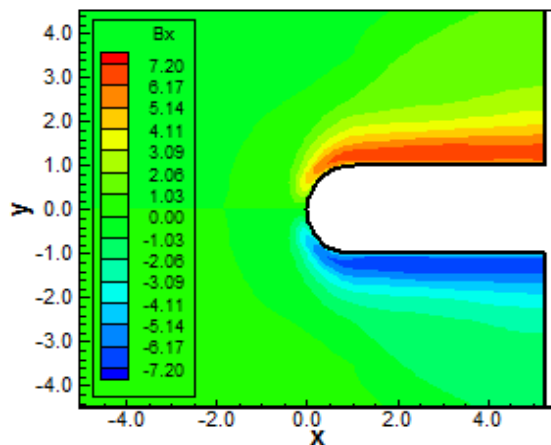
Figure 18: B_x component of the magnetic field (LGL-C83)
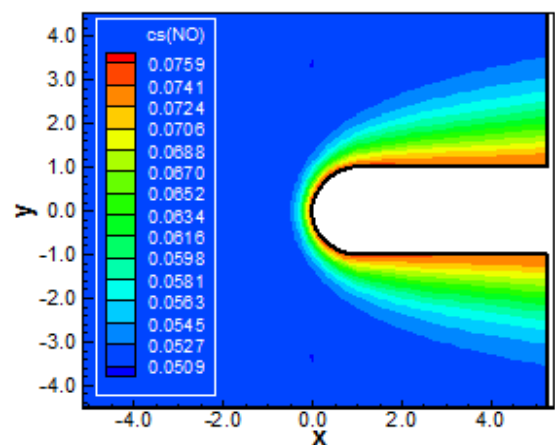
Figure 19: NO mass fraction contours (LGL-C83)

Wilcox (1988) Solutions
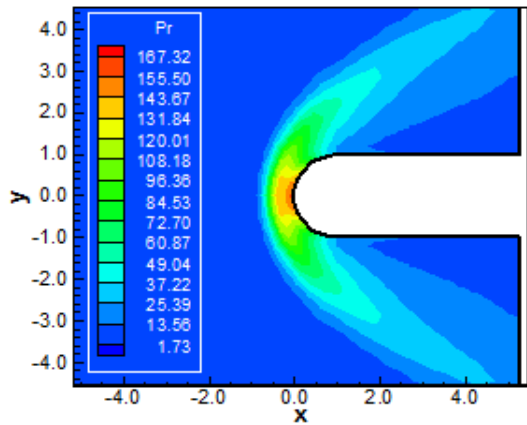
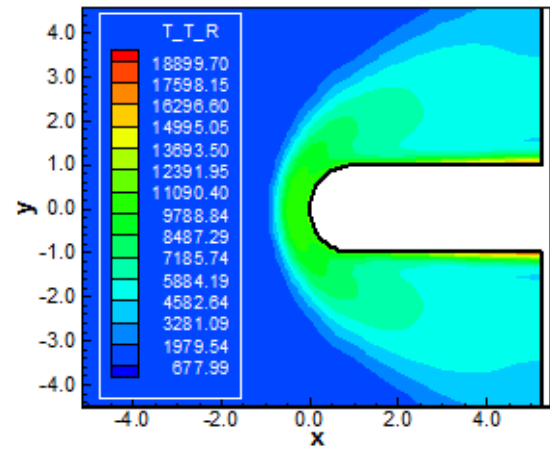*Figure 20: Pressure contours (CGR-W88)*
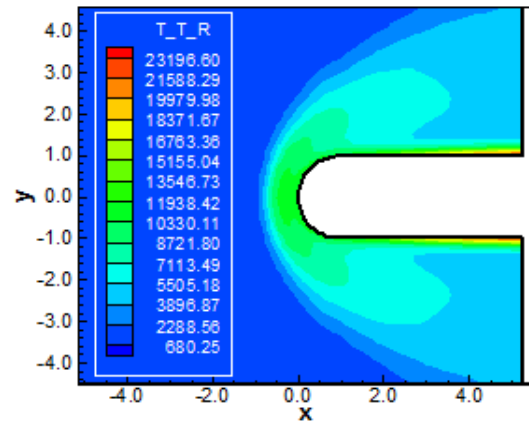
Figure 21: Translational/rotational temperature contours (CGR-W88)
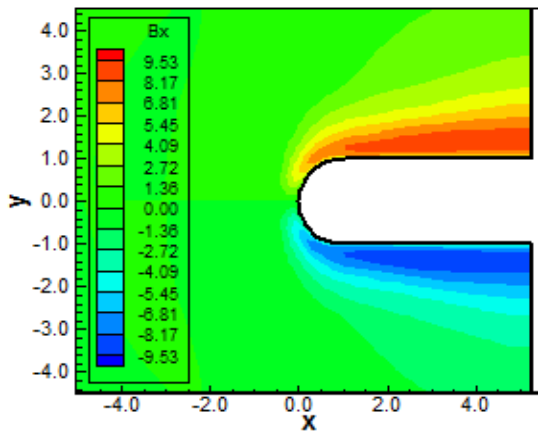
Figure 22: B_x component of the magnetic field (CGR-W88)
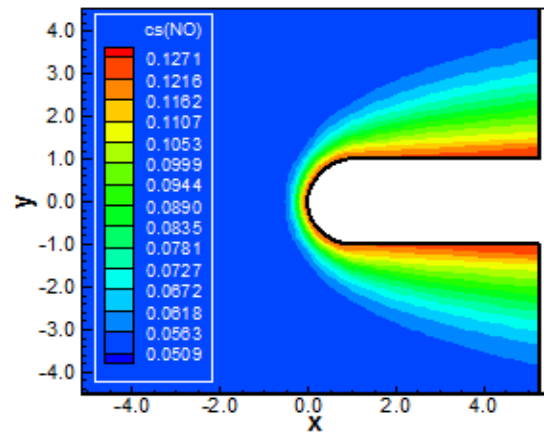
Figure 23: NO mass fraction contours (CGR-W88)
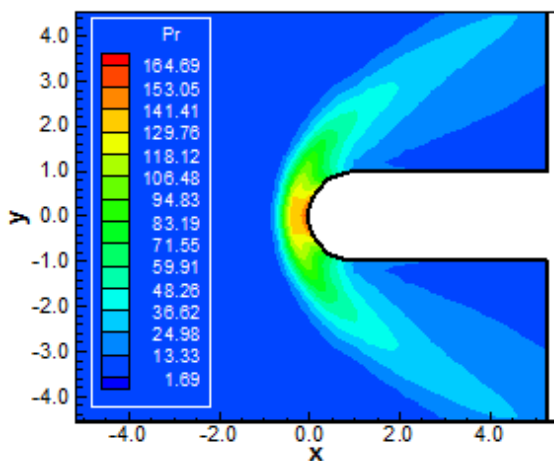
Figure 24: Pressure contours (CGL-W88)
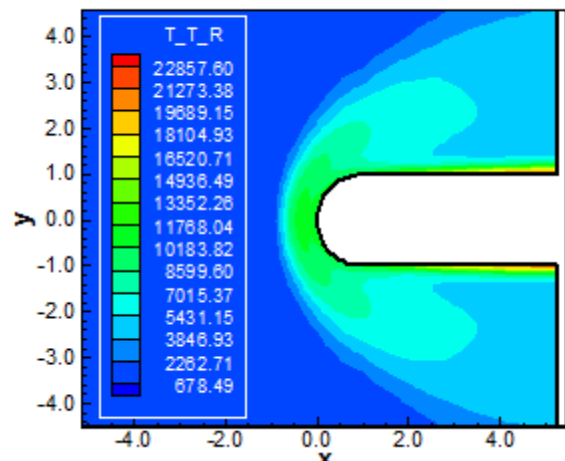
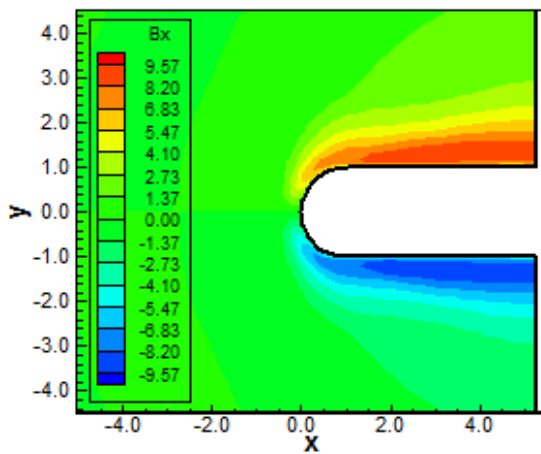*Figure 25: Translational/rotational temperature contours (CGL-W88)*
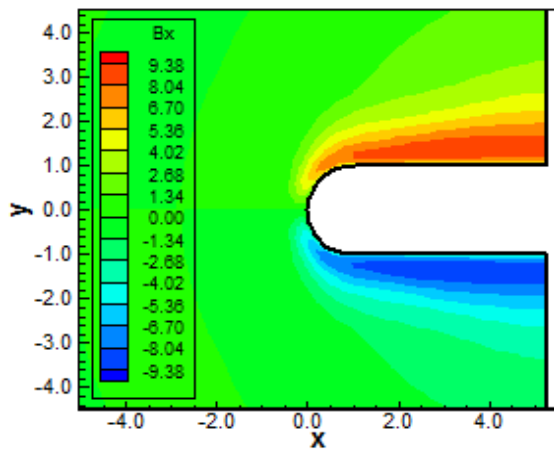
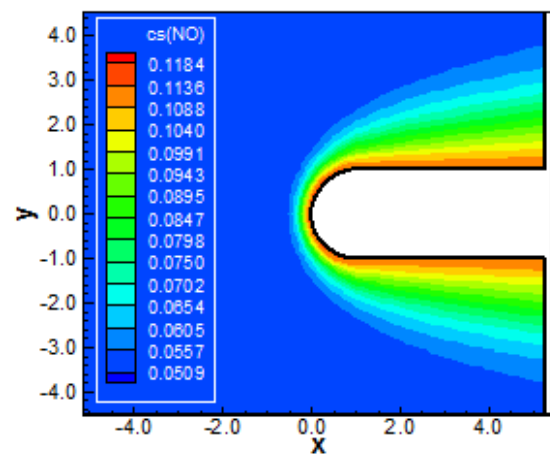*Figure 26: B_x component of the magnetic field (CGL-W88)*
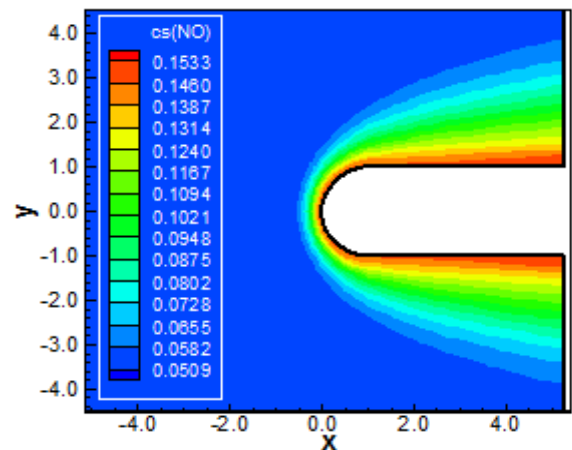
Figure 27: NO mass fraction contours (CGL-W88)
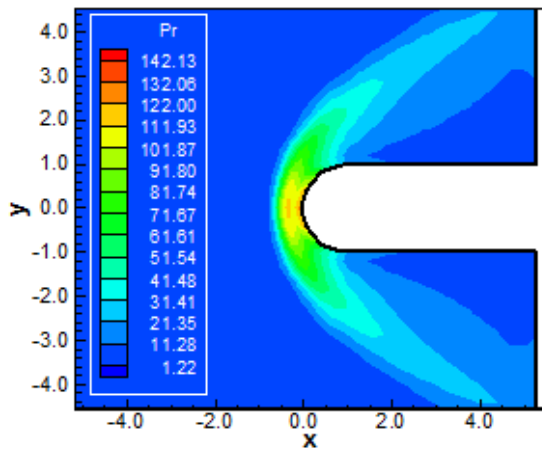
Figure 28: Pressure contours (LGR-W88)
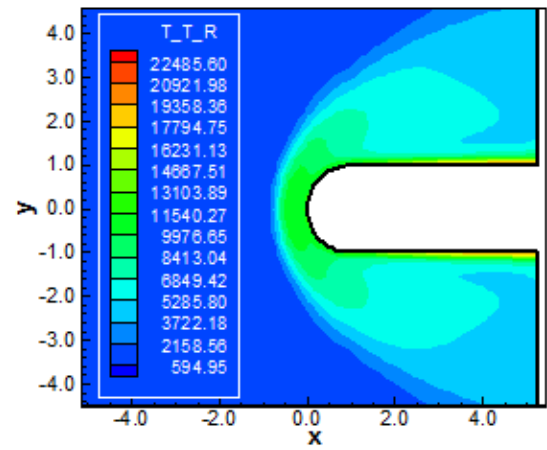
Figure 29: Translational/rotational temperature contours (LGR-W88)
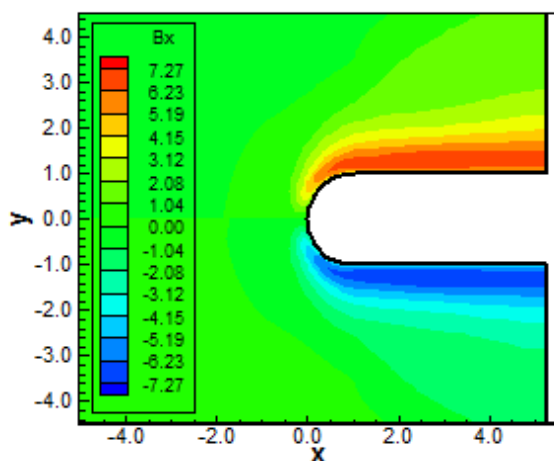
Figure 30: B_x component of the magnetic field (LGR-W88)
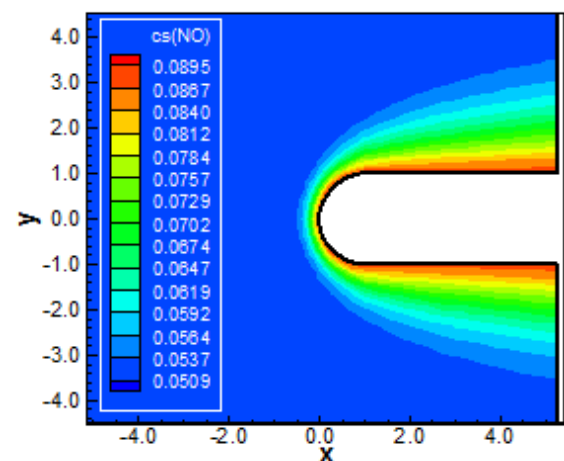
Figure 31: NO mass fraction contours (LGR-W88)
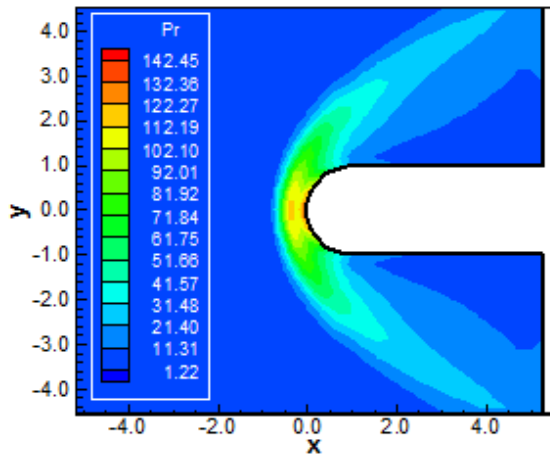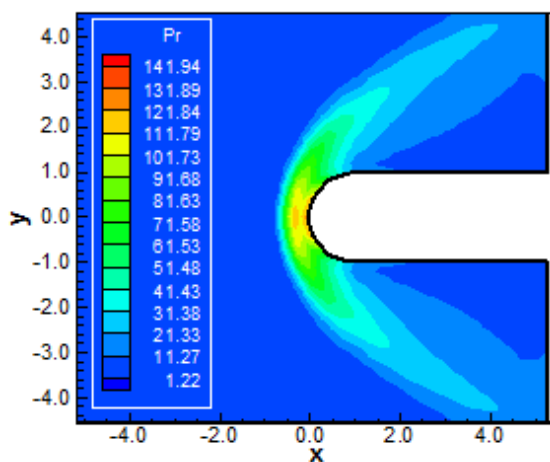
Figure 32: Pressure contours (LGL-W88)
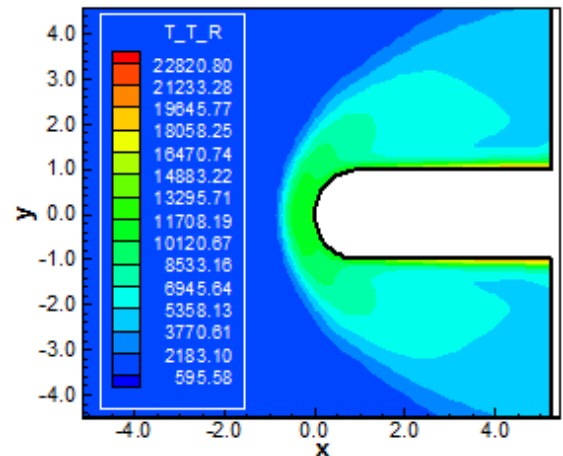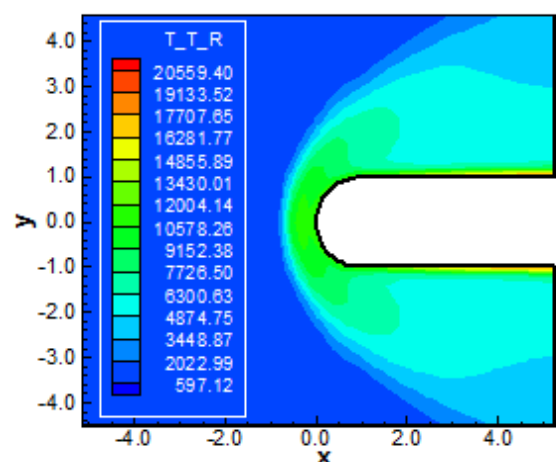

Figure 33: Translational/rotational temperature contours (LGL-W88)
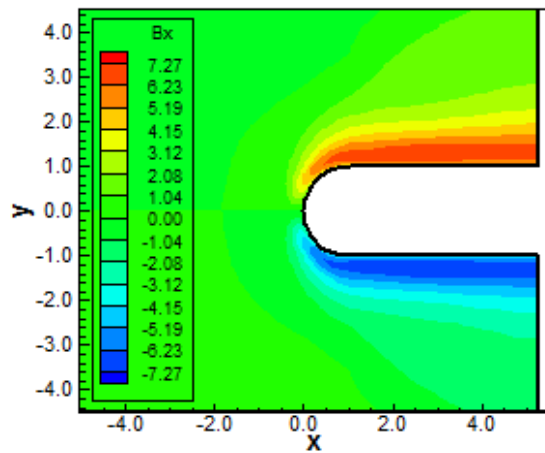
Figure 34: B_x component of the magnetic field (LGL-W88)
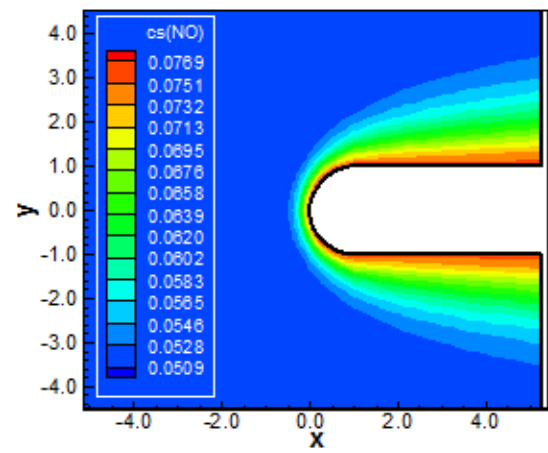
Figure 35: NO mass fraction contours (LGL-W88)

Yoder, Georgiadids and Orkwis (1996) Solutions
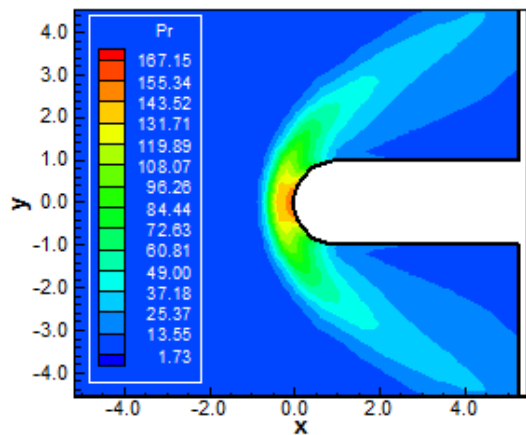
Figure 36: Pressure contours (CGR-YGO96)
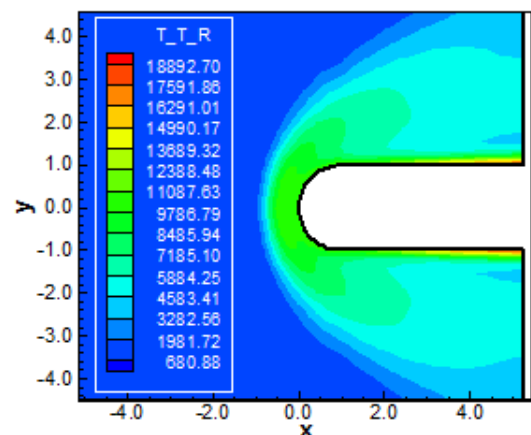
Figure 37: Translational/rotational temperature contours (CGR-YGO96)
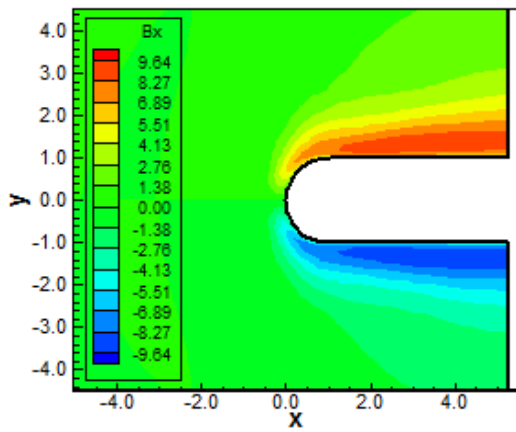
Figure 38: B_x component of the magnetic field (CGR-YGO96)
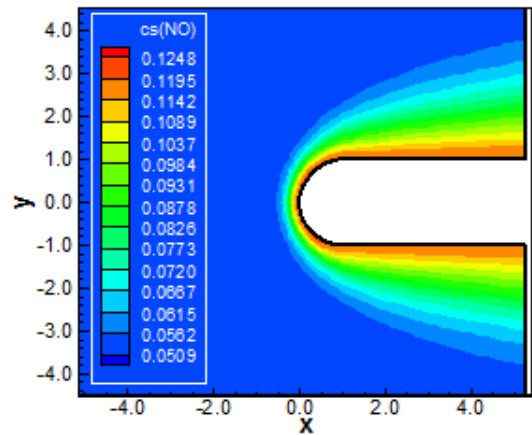
Figure 39: NO mass fraction contours (CGR-YGO96)
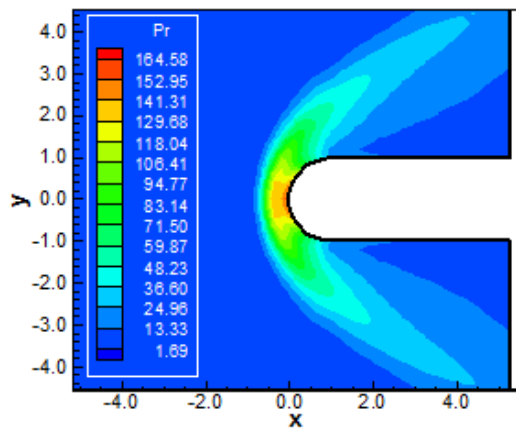
Figure 40: Pressure contours (CGL-YGO96)
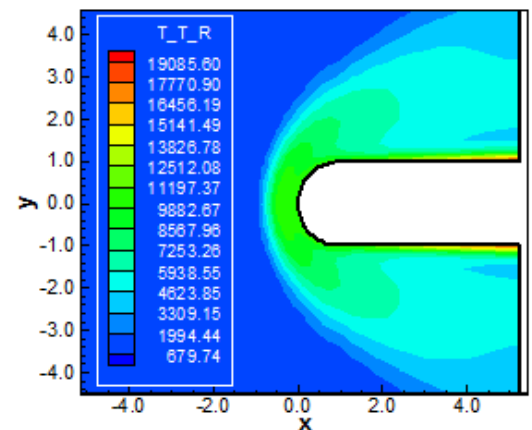
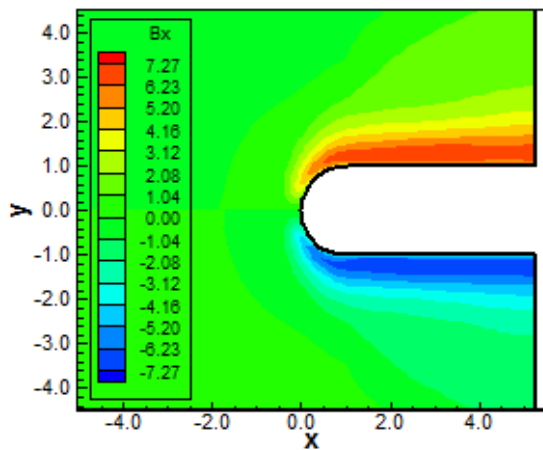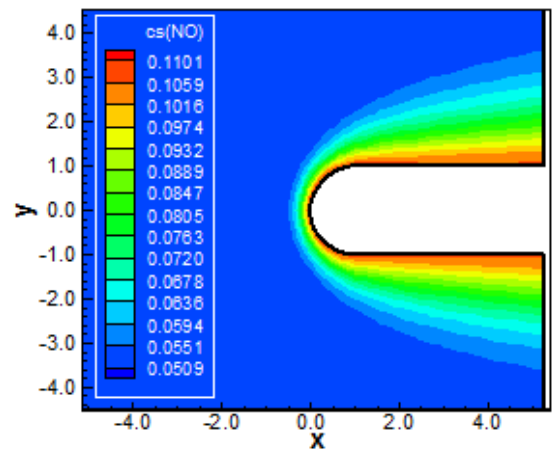*Figure 41: Translational/rotational temperature contours (CGL-YGO96)*
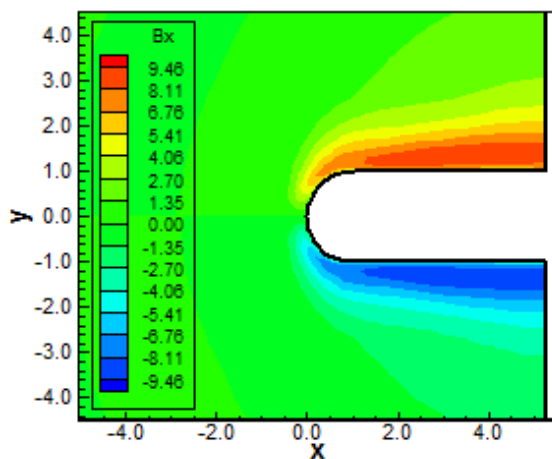
Figure 42: B_x component of the magnetic field (CGL-YGO96)
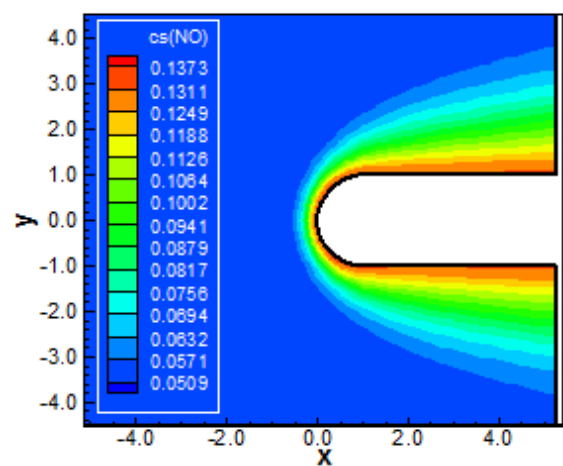
Figure 43: NO mass fraction contours (CGL-YGO96)
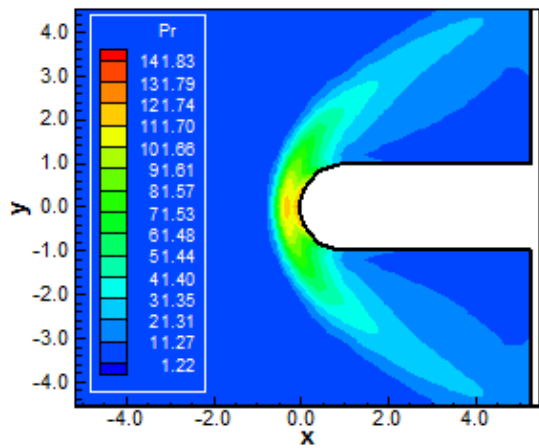
Figure 44: Pressure contours (LGR-YGO96)

Figure 45: Translational/rotational temperature contours (LGR-YGO96)

Figure 46: B_x component of the magnetic field (LGR-YGO96)
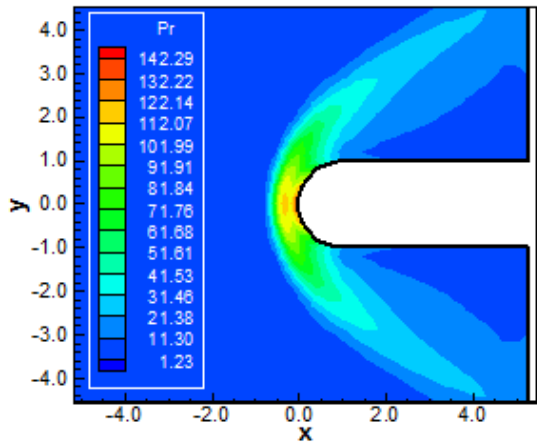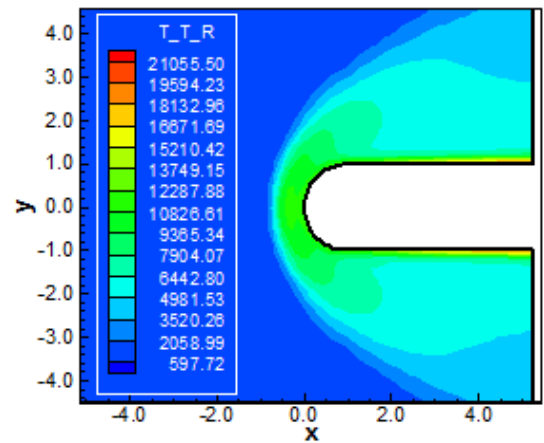

Figure 47: NO mass fraction contours (LGR-YGO96)

Figure 48: Pressure contours (LGL-YGO96)

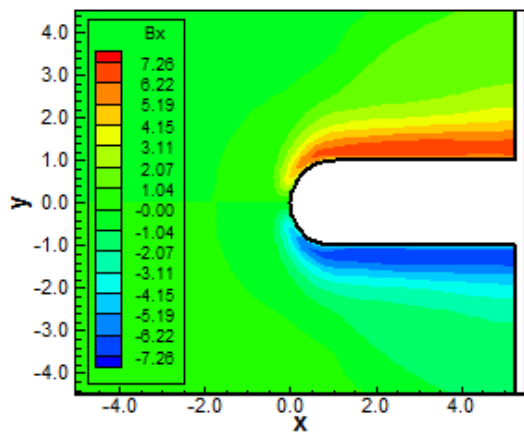*Figure 49: Translational/rotational temperature contours (LGL-YGO96)*

Figure 50: B_x component of the magnetic field (LGL-YGO96)

Figure 51: NO mass fraction contours (LGL-YGO96)

Coakley (1997) Solutions

Figure 52: Pressure contours (CGR-C97)

Figure 53: Translational/rotational temperature contours (CGR-C97)

Figure 54: B_x component of the magnetic field (CGR-C97)

Figure 55: NO mass fraction contours (CGR-C97)

Figure 56: Pressure contours (CGL-C97)

Figure 57: Translational/rotational temperature contours (CGL-C97)

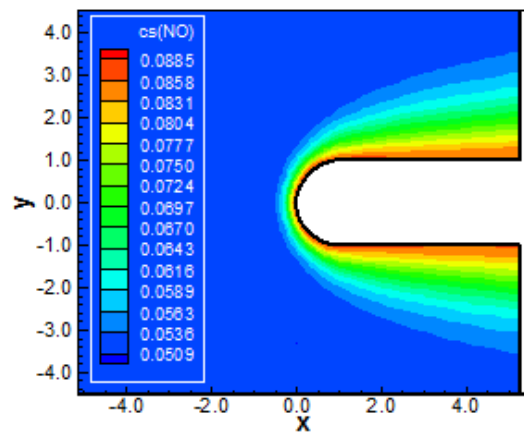Figure 58: B_x component of the magnetic field (CGL-C97)

Figure 59: NO mass fraction contours (CGL-C97)

Figure 60: Pressure contours (LGR-C97)

Figure 61: Translational/rotational temperature contours (LGR-C97)

Figure 62: B$_x$ component of the magnetic field (LGR-C97)

Figure 63: NO mass fraction contours (LGR-C97)

Figure 64: Pressure contours (LGL-C97)

Figure 65: Translational/rotational temperature contours (LGL-C97)

Figure 66: B$_x$ component of the magnetic field (LGL-C97)

Figure 67: NO mass fraction contours (LGL-C97)

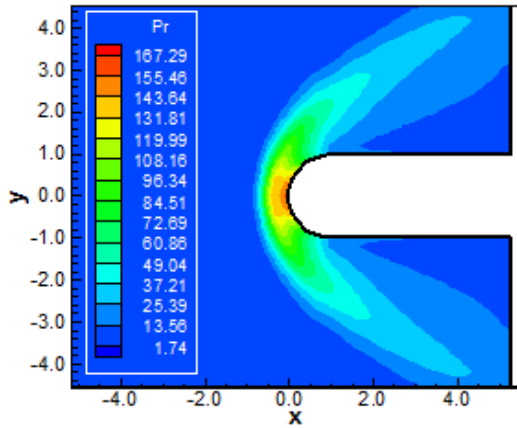**Rumsey, Gatski, Ying and Bertelrud (1998) Solutions**
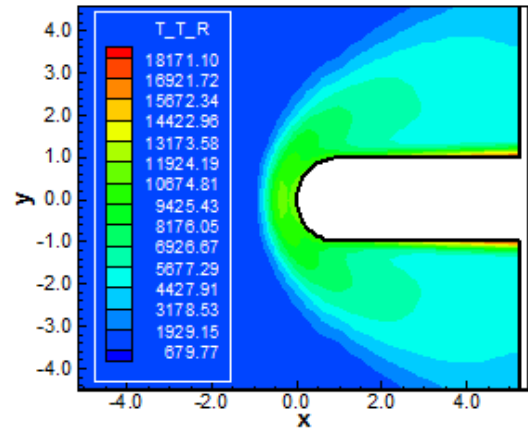

Figure 68: Pressure contours (CGR-RGYB98)

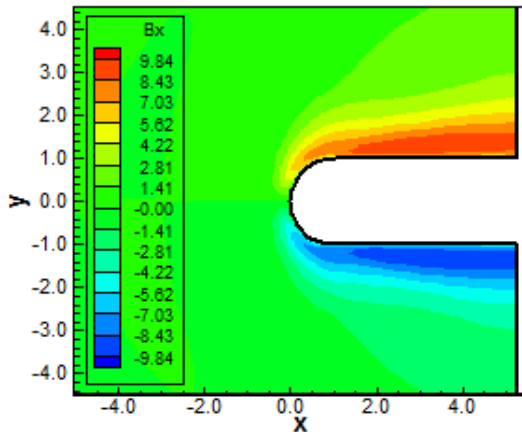*Figure 69: Translational/rotational temperature contours (CGR-RGYB98)*

Figure 70: B_x component of the magnetic field (CGR-RGYB98)
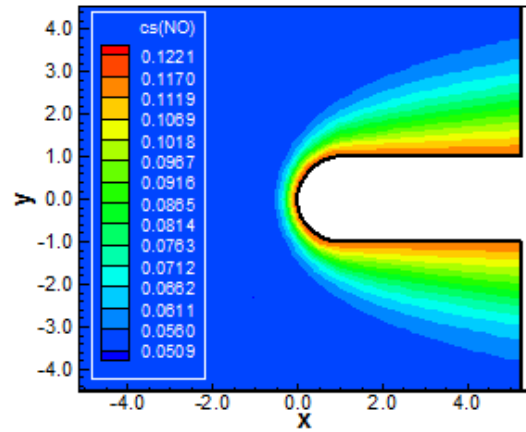

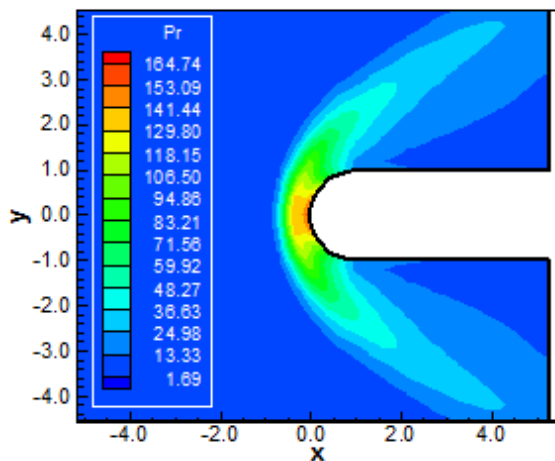*Figure 71: NO mass fraction contours (CGR-RGYB98)*

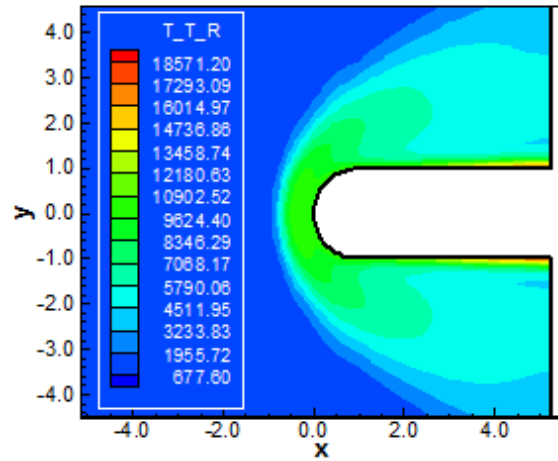*Figure 72: Pressure contours (CGL-RGYB98)*

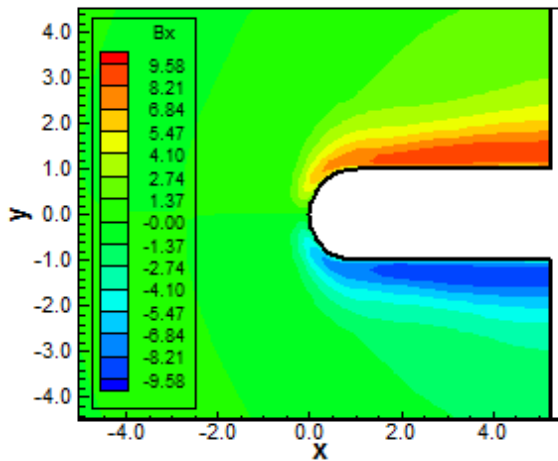*Figure 73: Translational/rotational temperature contours (CGL-RGYB98)*

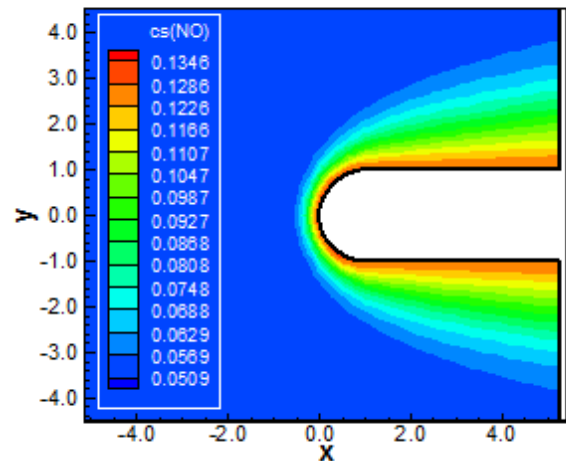*Figure 74: B_x component of the magnetic field (CGL-RGYB98)*

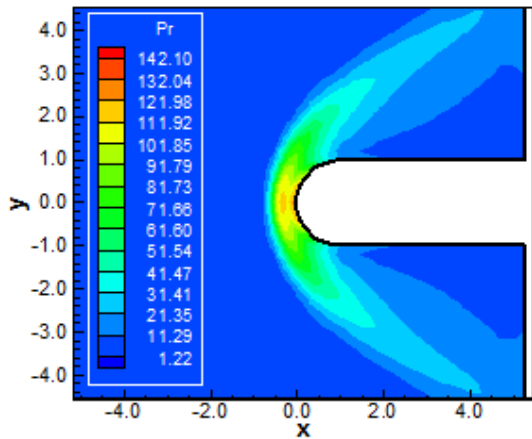*Figure 75: NO mass fraction contours (CGL-RGYB98)*

Figure 76: Pressure contours (LGR-RGYB98)
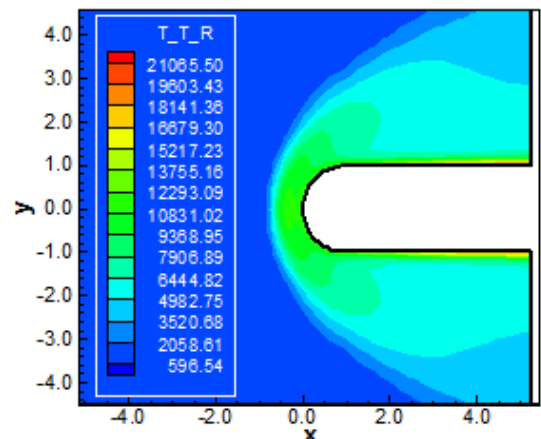

Figure 77: Translational/rotational temperature contours (LGR-RGYB98)
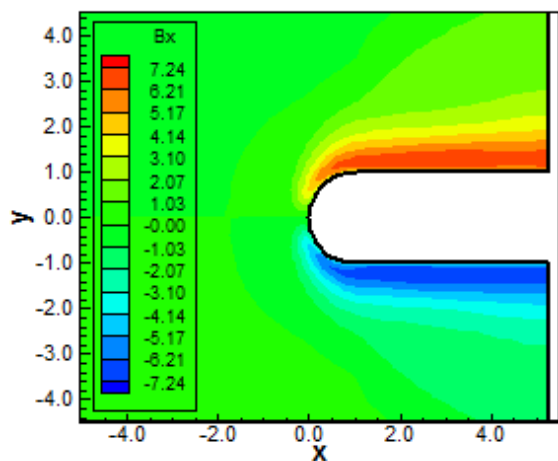

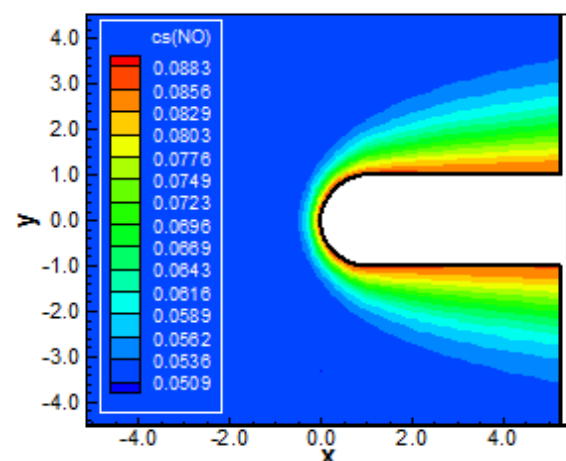*Figure 78: B_x component of the magnetic field (LGR-RGYB98)*

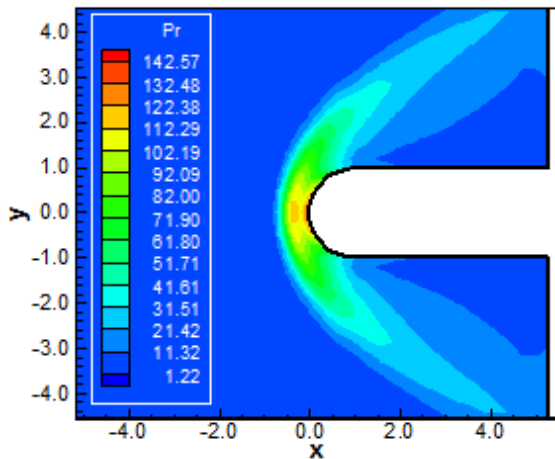*Figure 79: NO mass fraction contours (LGR-RGYB98)*

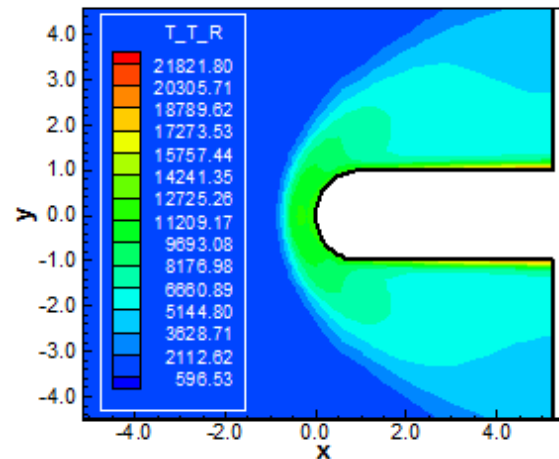*Figure 80: Pressure contours (LGL-RGYB98)*

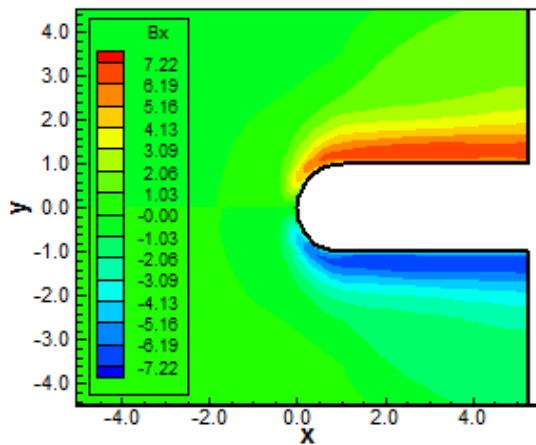*Figure 81: Translational/rotational temperature contours (LGL-RGYB98)*

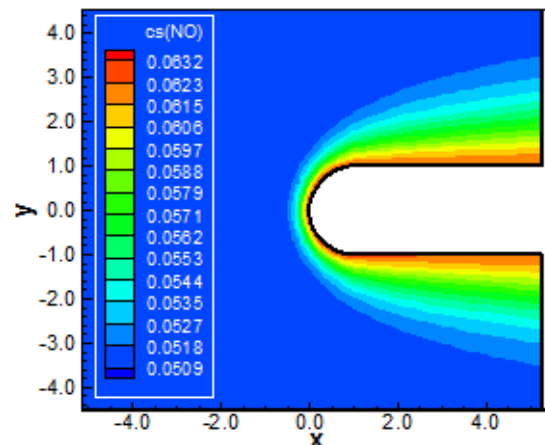*Figure 82: B_x component of the magnetic field (LGL-RGYB98)*

Figure 83: NO mass fraction contours (LGL-RGYB98)

11. Conclusions

In this work, a study involving a spectral method to solve the reactive Favre averaged Navier-Stokes equations, coupled with a turbulence model and the Maxwell equations, was performed. The Favre averaged Navier-Stokes equations coupled with the Maxwell equations, in conservative and finite volume contexts, employing structured spatial discretization, were studied. Turbulence was taken into account considering the implementation of five k-ω two-equation turbulence models, based on the works of [28-32].The numerical algorithm of Maciel was used to perform the reentry flow numerical experiments, which gave us an original contribution to the CFD community. Two types of numerical dissipation models were applied, namely: [61-62]. The "hot gas" hypersonic flow around a blunt body, in two-dimensions, was simulated. The convergence process was accelerated to steady state condition through a spatially variable time step procedure, which had proved effective gains in terms of computational acceleration ([42-43]). The Euler backward method was applied to march the scheme in time. The reactive simulations involved Earth atmosphere chemical model of seven species and eighteen reactions, based on the [44] model. The work of [40-41] was the reference one to present the fluid dynamics and Maxwell equations of electromagnetism based on a conservative and finite volume formalisms.The results have indicated that the Chebyshev collocation point variants were more accurate in terms of stagnation pressure estimations. For the studied problem such errors were inferior to 3.68%, being 1.93% the

best result. The Legendre collocation point variants were more accurate in terms of the lift coefficient estimations. Moreover, the Legendre colloaction point variants were more computationally efficient and cheaper.

As final conclusion, it was possible to highlight that, for the studied problem, the Maciel scheme coupled with the [28] turbulence model using Chebyshev-Gauss-Radau collocation points had the best performance in estimating the stagnation pressure, and the lift aerodynamic coefficient was better estimated by the Maciel scheme as using the Legendre-Gauss-Radau collocation points also coupled with the [28] turbulence model. Moreover, the best performance of the numerical scheme, for the 16th order of accuracy, was coupled with the [31] turbulence model, when using the Legendre-Gauss-Radau collocation points, employing a CFL of 0.10, and converging in 1,464 iterations.

Finally, to close this work, the computational cost of the numerical scheme using the several types of collocation points was presented in Tabs. 7. For the 16th order of accuracy, the cheapest combination was the Maciel scheme coupled with [28] turbulence model and using Legendre-Gauss-Lobatto collocation points with a cost of 0.0019667 sec/per-volume/per-iteration.

References

[1]. Barnes CJ, Huang GP, Shang JS. A high resolution spectral method for the compressible Navier-Stokes equations. AIAA Paper 2011-0049; 2011.

[2]. Huang P, Wang ZJ, Liu Y. An implicit space-time spectral difference method for discontinuity capturing using adaptive polynomials. AIAA Paper 2005-5255; 2005.

[3]. Huang P. High order discontinuity capturing using adaptive polynomials. AIAA Paper 2006-0305; 2006.

[4]. Steger JL, Warming RF. Flux vector splitting of the inviscid gasdynamic equations with application to finite difference methods. Journal of Computational Physics, 1981; 40: 263-293.

[5]. Hughes T. The finite element method, linear static and dynamic finite element analysis. Prentice-Hall, Inc.

[6]. Lele S. Compact finite difference schemes with spectral-like resolution. Journal of Computational Physics, 1991; 103: 16-42.

[7]. Gottlieb D, Orszag S. Numerical analysis of spectral methods: theory and applications. Society for Industrial and Applied Mathematics, Philadelphia.

[8]. Hussaini MY, Kopriva DA, Salas MD, Zang TA. Spectral methods for the Euler equations: Part I – Fourier methods and shock capturing. AIAA Journal, 1985; 23(1): 64-70.

[9]. Slater JC. Electronic energy bands in metal. Physical Review, 1934; 45: 794-801.

[10]. Barta J. Über die naherungsweise 1üsung einigerzweidimensionalerelastizität saufgaben. ZeitschriftfuerAngewandteMathematik und Mechanik, 1937; 17: 184-185.

[11]. Frazer RA, Jones WP, Skan SW. Approximation to functions and to the solutions of differential equations. Aeronautical Research Council, London. R&M 1799; 1937.

[12]. Lanczos CL. Trigonometric interpolation of empirical and analytic functions. Journal of Mathematics and Physics, 1938; 17: 123-199.

[13]. Gottlieb D, Lustman L, Orszag SA. Spectral calculations of one-dimensional inviscid compressible flows. SIAM Journal of Scientific and Statistical Computation, 1981; 2: 296-310.

[14]. Taylor TD, Meyers RB, Albert JH. Pseudospectral calculations of shock waves, rarefaction waves and contact surfaces. Computers and Fluids, 1981; 9: 469-473.

[15]. Zang TA, Hussaini MY. Mixed spectral-finite difference approximations for slightly viscous flows. Proceedings of the 7th International Conference on Numerical Methods in Fluid Dynamics. Edited by W. C. Reynolds and R. W. MacCormack.Lecture Notes in Physics, Springer-Verlag, New York, 1981; (141): 461-466.

[16]. Narayan JR, Girimaji SS. Turbulent reacting flow computations including turbulence-chemistry interactions.AIAA Paper 92-0342; 1992.

[17]. Gnoffo PA, Gupta RN, Shinn JL. Conservation equations and physical models for hypersonic flows in thermal and chemical nonequilibrium. NASA TP 2867; 1989.

[18]. Liu M, Vinokur M. Upwind algorithms for general thermo-chemical nonequilibrium flows.AIAA Paper 89-0201; 1989.

[19]. Park C. Radiation enhancement by nonequilibrium in Earth's atmosphere. Journal of Spacecraft and Rockets, 1985; 22(1): 27-36.

[20]. Park C. Problem of rate chemistry in the flight regimes of aeroassissted orbital transfer vehicles. Thermal design of aeroassissted orbital transfer vehicles. Progress in Astronautics and Aeronautics. Edited by H. F. Nelson, AIAA, NY, 1985; 96: 511-537.

[21]. Gnoffo PA. Three-dimensional AOTV flowfields in chemical nonequilibrium. AIAA Paper 86-0230; 1986.

[22]. Li CP. Implicit methods for computing chemically reacting flow. NASA TM-58274; 1986.

[23]. Lee JH. Basic governing equations for the flight regimes of aeroassisted orbital transfer vehicles. Thermal design of aeroassisted transfer vehicles. Progress in Astronautics and Aeronautics, AIAA, 1985; 96: 3-53.

[24]. Park C. Convergence of computation of chemically reacting flows. Thermophysical aspects of reentry flows. Progress in Astronautics and Aeronautics. Edited by J. N. Moss and C. D. Scott, AIAA, NY, 1986; 103: 478-513.

[25]. Park C. Assessment of two-temperature kinetic model for dissociating and weakly-ionizing Nitrogen. AIAA Paper 86-1347; 1986.

[26]. Park C. Calculation of nonequilibrium radiation in the flight regimes of aeroassissted orbital transfer vehicles. Thermal design of aeroassissted orbital transfer vehicles. Progress in Astronautics and Aeronautics. Edited by H. F. Nelson, AIAA, NY, 1985; 96: 395-418.

[27]. Park C. Nonequilibriumair radiation (NEQAIR) program: User's manual. NASA TM-86707; 1985.

[28]. Coakley TJ. Turbulence modeling methods for the compressible Navier-Stokes equations. AIAA Paper 83-1693; 1983.

[29]. Wilcox DC. Reassessment of the scale-determining equation for advanced turbulence models. AIAA Journal, 1988; 26(11): 1299-1310.

[30]. Yoder DA, Georgiadids NJ, Orkwis PD. Implementation of a two-equation k-omega turbulence model in NPARC. AIAA Paper 96-0383; 1996.

[31]. Coakley TJ. Development of turbulence models for aerodynamic applications. AIAA Paper 97-2009; 1997.

[32]. Rumsey CL, Gatski TB, Ying SX, Bertelrud A. Prediction of high-lift flows using turbulent closure models. AIAA Journal, 1998; 36(5): 765-774.

[33]. Davidson PA. Magnetohydrodynamics in materials processing. Ann. Rev. Fluid Mech.1999; 31: 273-300.

[34]. Ziemer RW, Bush WB. Magnetic field effects on bow shock stand-off distance. Physical Review Letters.1958; 1(2): 58-59.

[35]. Meyer RX. Magnetohydrodynamics and aerodynamic heating. ARS Journal.1959; 29(3): 187-192.

[36]. Gurijanov EP, Harsha PT. AJAX: New directions in hypersonic technology. AIAA Paper 96-4609; 1996.

[37]. Brichkin DI, Kuranov AL, Sheikin EG. MHD-technology for scramjet control. AIAA Paper 98-1642; 1998.

[38]. Ganiev YC, Gordeev VP, Krasilnikov AV, Lagutin VI, Otmennikov VN, Panasenko AV. Theoretical and experimental study of the possibility of reducing aerodynamic drag by employing plasma injection. AIAA Paper 99-0603; 1999.

[39]. Adamovich IV, Subramanian VV, Rich JW, Macheret SO. Phenomenological analysis of shock-wave propagation in weakly ionized plasmas. AIAA Journal. 1998; 36(5): 816-822

[40]. Gaitonde DV. Development of a solver for 3-D non-ideal magnetogasdynamics. AIAA Paper 99-3610; 1999.

[41]. Maciel ESG. Magnetic formulation and first-order schemes in 2D and 3D – Euler, Navier-Stokes and Maxwell equations in 2D and 3D – Perfect gas formulation. Saarbrücken, Deutschland: Lambert Academic Publishing (LAP), 2015; Ch. 7: 225-290.

[42]. Maciel ESG. Simulations in 2D and 3D applying unstructured algorithms, Euler and Navier-Stokes equations – Perfect gas formulation. Saarbrücken, Deutschland: Lambert Academic Publishing (LAP), 2015; Ch. 1: 26-47.

[43]. Maciel ESG. Simulations in 2D and 3D applying unstructured algorithms, Euler and Navier-Stokes equations – Perfect gas formulation. Saarbrücken, Deutschland: Lambert Academic Publishing (LAP), 2015; Ch. 6: 160-181.

[44]. Blottner FG. Viscous shock layer at the stagnation point with nonequilibriumair chemistry. AIAA Journal, 1969; 7(12): 2281-2288.

[45]. Hussaini MY, Streett CL, Zang TA. Spectral methods for partial differential equations. ICASE Report No. 83-46; 1983.

[46]. Davis PA, Rabinowitz P. Numerical integration. Blaisdell Publishing Co.; 1967.

[47]. Canuto C, Hussaini MY, Quarteroni A, Zang TA. Spectral methods evolution to complex geometries and applications to fluid dynamics. Scientific Computation Springer; 2007.

[48]. Narayan JR. Computation of compressible reacting flows using a two-equation turbulence model. Proceedings of the 4th International Symposium on Computational Fluid Dynamics, Davis, California, September, 1991.

[49]. Williams FA. Combustion theory, Addison-Wesley Publishing Company, Inc., Reading, MA, 1965.

[50]. Drummond JP, Carpenter MH, Riggins DW. Mixing and mixing enhancement in supersonic reacting flows. High speed propulsion systems: Contributions to thermodynamic analysis. Ed. E. T. Curran and S. N. B. Murthy, American Institute of Astronautics and Aeronautics (AIAA), Washington, D. C., 1990.

[51]. Maciel ESG. Hypersonic reactive flow simulations in two-dimensions, chemical and thermochemical non-equilibrium conditions. Saarbrücken. Deutschland: Lambert Academic Publishing (LAP), 2015; Ch. 5: 333-406.

[52]. Maciel ESG. Hypersonic reactive flow simulations in two-dimensions, chemical and thermochemical non-equilibrium conditions. Saarbrücken. Deutschland: Lambert Academic Publishing (LAP), 2015; Ch. 6: 407-490.

[53]. Favre A. Statistical equations of turbulent gases, Institut de MechaniqueStatistique de la Turbulence, Marseille.

[54]. Maciel ESG. Turbulent thermochemical non-equilibrium reentry flows in 2D. Computational and Applied Mathematics Journal, 2015; 1(4): 201-224.

[55]. Prabhu RK. An implementation of a chemical and thermal nonequilibrium flow solver on unstructured meshes and application to blunt bodies. NASA CR-194967; 1994.

[56]. Saxena SK, Nair MT. An improved Roe scheme for real gas flow. AIAA Paper 2005-0587; 2005.

[57]. Maciel ESG, Andrade CR. Turbulent chemical non-equilibrium reentry flows in 2D - Five species. Asian Journal of Mathematics and Computer Research, 2017; 20(3): 130-168.

[58]. Maciel ESG, Andrade CR. Turbulent thermochemical non-equilibrium reentry flows with magnetic actuation in 2D – Seven species, Asian Journal of Physical and Chemical Sciences, 2017; 3(4): 1-36.

[59]. Ait-Ali-Yahia D, Habashi WG. Finite element adaptive method for hypersonic thermochemical nonequilibriumflows. AIAA Journal.1997; 35(8): 1294-1302.

[60]. Long LN, Khan MMS, Sharp HT. Massively parallel three-dimensional Euler / Navier-Stokes method. AIAA Journal. 1991; 29(5): 657-666.

[61]. Mavriplis DJ. Accurate multigrid solution of the Euler equations on Unstructured and Adaptive Meshes. AIAA Journal, 1990; 28(2): 213-221.

[62]. Turkel E, Vatsa VN. Effect of artificial viscosity on three-dimensional flow solutions.AIAA Journal, 1994; 32(1): 39-45, 1994.

[63]. Vincent WG, Kruger Jr. CH. Introduction to physical gas dynamics. Malabar, Florida, EUA: Krieger Publishing Company. 2002; Ch. 1: 1-26.

[64]. Fox RW, McDonald AT. Introdução à mecânica dos fluidos. Guanabara Editor; 1988.

[65]. Maciel ESG. Simulação numérica de escoamentos supersônicos e hipersônicos utilizando técnicas de dinâmica dos fluidos computacional. DoctoralThesis. ITA, CTA, São José dos Campos, SP, Brazil; 2002.

[66]. Anderson Jr. JD. Fundamentals of aerodynamics. McGraw-Hill, Inc., 5th Edition, 1008p.; 2010.